

# Characterizing Gravitational Wave Detector Networks: From A<sup>#</sup> to Cosmic Explorer

Cosmic Explorer White Paper Team<sup>1</sup>

<sup>1</sup>*The Milkyway, The Universe*

## CONTENTS

I. Introduction	1
II. Gravitational-Wave Observatory Network Configurations	3
III. Population of compact binaries	3
A. Binary black holes	3
1. Local population	4
2. Population III black holes	4
3. Primordial black holes	4
4. Intermediate mass binary black holes (IMBBHs)	5
B. Binary neutron stars	5
C. Neutron star-black hole mergers	5
IV. Detection and parameter estimation of the populations	5
A. Detection efficiency and detection rate	6
B. Measurement uncertainty of source parameters	9
C. 3D localization of sources	13
V. Open Science Questions Uniquely Address by Gravitational-Wave Observations	22
A. Black holes and neutron stars throughout the cosmos	22
B. Multimessenger astrophysics and dynamics of dense matter	22
1. Multimessenger observations and early warnings	22
2. Measuring the radius of the neutron star	23
C. New sources, new probes and extreme astrophysics	23
1. Continuous waves	23
2. Core collapse supernovae	24
3. Starquakes	25
D. Fundamental physics and precision measurement of the Hubble constant	25
1. Testing general relativity and fundamental physics	25
2. Measuring the Hubble constant with golden dark sirens and bright sirens	26
3. Measuring the $\Lambda$ CDM with NS tides	27
4. Measuring the dark energy with NS tides	27
5. <a href="#">Gravitational-wave lensing</a>	27
E. Dark matter, early universe and physics beyond the standard model	28
1. Stochastic backgrounds	28
F. Axion clouds around rotating black holes	30

## References

30

## I. INTRODUCTION

Over the past eight years since their first discovery, interferometric gravitational-wave detectors LIGO and Virgo have observed  $\sim \mathcal{O}(100)$  binary black hole and neutron star mergers [1]. The fourth (O4) and fifth (O5) observing runs over the next five to seven years will add hundreds more to the catalog of compact binary coalescences, and we can expect LIGO and Virgo, eventually joined by KAGRA and LIGO-India, to make many more discoveries. These detections will enable follow-up observations and multi-messenger astronomy, population inferences, dense matter physics and cosmology. The LIGO and Virgo collaborations have already developed plans for further improvements in sensitivity beyond O5 that will fully exploit what's possible at existing facilities. Accomplishing sensitivity levels significantly greater than those currently envisaged will require new facilities, with longer interferometer arms, but marginal improvements in detector technology, as described in the NSF-funded Horizon Study for the Cosmic Explorer project.

Gravitational-wave observations can address questions across multiple disciplines from general relativity to relativistic astrophysics, nuclear physics to dark matter searches and cosmology to beyond the standard model of particle physics. They can do this by observing binary black hole coalescences from an epoch when the universe was still assembling its first stars, binary neutron stars far beyond redshifts when the star formation in the Universe was at its peak, stochastic backgrounds produced in the primordial Universe, new sources and phenomena such as supernovae, stellar quakes and rapidly rotating neutron stars and, very likely, new phenomena and sources not imagined by anyone so far. To realize the full potential of gravitational-wave astronomy, it is necessary to build longer detectors with sensitivity levels that are at least an order of magnitude better than those of A+ detectors. In this paper we describe the science that can be accomplished at the limit of current facilities and how future observatories can vastly transform the field with new observatories, while answering many of the pressing problems in high energy physics, astronomy and cosmology. To this end we will consider eight different networks, each consisting of 3 detectors belonging to one of four classes: (1) 3 upgraded LIGO detectors, two in the US and one in India (0XG), (2) two upgraded LIGO detectors (in the US or India) together with one Cosmic Explorer observatory (1XG), (3) one upgraded LIGO detector (in the US or India) together with two next generation observatories

(2XG), (4) three next generation observatories (3XG).

A broad-brush summary of our findings is given in I.

Science Goal Requirements	Network Performance							
	No XG	1 XG			2 XG			3 XG
	HLA	HLET	20LA	40LA	20LET	40LET	4020A	4020ET
<b>BHs and NSs Throughout Cosmic Time</b>								
NS-NS rates, mass function, formation scenarios: # of NS-NS at $z \geq 1$ with $\delta z/z \leq 20\%$ and $(\delta m'_1/m'_1) \leq 30\%$	0	0	0	0	0	7	22	81
Unveiling the elusive population of IMBH: # of IMBHs at $z \geq 3$ with $\delta z/z \leq 20\%$ and $(\delta m'_1/m'_1) \leq 20\%$	6	429	151	193	840	865	514	888
BH-BH high- $z$ formation channels and mass function: # of BH-BH at $z \geq 10$ with $\delta z/z \leq 20\%$ and $(\delta m'_1/m'_1) \leq 20\%$	0	12	6	35	65	142	110	233
<b>MMA and Dynamics of Dense Matter</b>								
GW170817-like golden sample: # of NS-NS at $z \leq 0.06$ with $\Delta\Omega \leq 0.1 \text{ deg}^2$	0	0	0	0	0	1	1	7
r-process and kilonova-triggered follow up: # of NS-NS at $0.06 < z \leq 0.1$ with $\Delta\Omega \leq 1 \text{ deg}^2$	1	8	6	6	26	47	32	71
Jet afterglows (large FOVs and/or small-FOV mosaicking): # of NS-NS at $0.1 < z \leq 2$ with $\Delta\Omega \leq 10 \text{ deg}^2$	257	1040	783	892	6028	9200	3907	27180
Mapping GRBs to progenitors up to star-formation peak: # of NS-NS at $z > 2$ with $\Delta\Omega \leq 100 \text{ deg}^2$	0	2	19	37	6342	24974	3729	65537
Pre-merger alerts: # NS-NS with $\Delta\Omega \leq XX \text{ deg}^2 YY$ minutes before merger								
NS EoS constraints: # of NS-NS with $\text{SNR} \geq 100$ # of NS with $\Delta R < 0.1 \text{ km}$	0	44	24	156	92	256	268	376
<b>New Probes of Extreme Astrophysics</b>								
# Isolated NSs with $\text{SNR} > XX$ # Accreting NSs with $\text{SNR} > XX$ Galactic SN SNR range SGR giant flare $D_{\text{max}}$ (pc) Long-duration post-merger $d_{\text{max}}$ (pc)								
<b>Fundamental Physics and Precision Cosmology</b>								
Graviton mass: # of NS-NS at $z \geq 5$ # of BH-BH at $z \geq 5$	0 19	0 2522	0 2203	84 3916	0 3790	336 4678	584 4506	880 5121
Probing rare events: # of BH-BH with $\text{SNR} > 100$ # of BH-BH with $\text{SNR} > 1000$	17 0	1897 0	1300 1	5000 3	3716 0	7453 2	6900 4	9485 3
Precision tests of GR (IMR and QNM): Effective SNR of BH-BH Effective SNR for post-inspiral # of BH-BH with post-inspiral $\text{SNR} > 100$	2.4e3 1.9e3 6	1.1e4 5.8e3 314	9.8e3 5.3e3 286	1.6e4 8.1e3 1190	1.5e4 7.7e3 788	2.0e4 9.9e3 1859	1.9e4 9.5e3 1751	2.2e4 1.1e4 2486
$H_0$ and tests of GR: # of NS-NS with $\delta d_L/d_L \leq 10\%$ and $\Delta\Omega \leq 10 \text{ deg}^2$ # of NS-NS with $z \leq 0.5$ , $\delta d_L/d_L \leq 10\%$ and $\Delta\Omega \leq 10 \text{ deg}^2$ # of BH-BH with $\delta d_L/d_L \leq 10\%$ and $\Delta\Omega \leq 1 \text{ deg}^2$	14 14 69	269 269 489	63 63 287	71 71 346	1111 1111 2177	1579 1568 3274	785 784 1329	4801 4265 6746
<b>Dark Matter and the Early Universe</b>								
Dark matter in NSs: NS-NS with $\delta t_{\text{collapse}}/t_{\text{collapse}} \leq XX(\%)$ Ultra-light Boson field: $\Omega_{\text{GW}}$ detectable in 1yr with $\text{SNR}=3$ at $f_{\text{ref}} = 25 \text{ Hz}$ , $\alpha = 0$	1.99 $\times 10^{-10}$	3.05 $\times 10^{-12}$	5.41 $\times 10^{-11}$	3.05 $\times 10^{-11}$	2.62 $\times 10^{-12}$	2.05 $\times 10^{-12}$	5.63 $\times 10^{-12}$	1.85 $\times 10^{-12}$

Table I: This table is not intended to appear in the final version of the WP. We will convert numbers here into figures. This Table when finalized could be added to a CE technical note.

The rest of the paper is organized as follows.

## II. GRAVITATIONAL-WAVE OBSERVATORY NETWORK CONFIGURATIONS

The previous section listed the science questions. In this Section we will summarize the list of gravitational-wave detectors that are expected to be available over the next two decades to address those questions. We start with detectors with the best sensitivities that could be installed in LIGO facilities, followed by networks that include one or more XG observatories consisting of CE and/or ET. The collection of network configurations studied is intended to be sufficiently broad without being unduly complex: broad enough to gauge all plausible network configurations but not so complex as to consider every possible scenario. Indeed, we are aided by research indicating that the critical feature of a future gravitational-wave network is the number of next-generation detectors present, while their locations are of secondary importance [1]. To this end, we consider the following observatories:

Detector	Latitude	Longitude	Orientation
CE A	46°00'00"	-125°00'00"	260.0°
CE B	29°00'00"	-94°00'00"	200.0°
ET	40°31'00"	+9°25'00"	90.0°
LLO	30°33'46.4196"	-90°46'27.2654"	197.7165°
LHO	46°27'18.5280"	-119°24'27.5657"	125.9994°
LAO	19°36'47.9017"	+77°01'51.0997"	117.6157°

Table II. Position and orientation of the detectors. Latitudes (Longitudes) are positive in the northern hemisphere (East of the Greenwich meridian). The orientation is the angle north of east of the  $x$ -arm (Note: here we follow the same convention used in Bilby [], which is different from what used in Refs [], where the orientations of the detectors are clockwise rotations from the local north). For L-shaped detectors, the  $x$ -arm is defined as the one that completes a right-handed coordinate systems together with the other arm and the local, outward, vertical direction. For ET, the  $x$ -arm is defined such that the two other arms lay westward of it.

### a. Cosmic Explorer Observatories (CE A, CE B)

Since the locations of the CE observatories have yet to be determined, we selected two fiducial locations for CE; CE A off the coast of Washington state, and CE B off the coast of Texas. These locations are intentionally unphysical to avoid impacting our ability to find a potential home for CE, but close enough to a wide range of potential sites to be representative from the point of view of gravitational-wave science (see Table II). The CE A location is considered in both the 40 km and the 20 km lengths, while the CE B location hosts only a 20 km observatory. The strain sensitivity of the two choices is shown in Fig. 1

### b. Existing LIGO Sites (LHO, LLO, LAO)

In order to focus on the science enabled by CE beyond what

Number of XG Observatories	Network Name	Detectors in the network
None	HLA	LHO, LLO, LAO
1 XG	40LA	CE A 40 km, LLO, LAO
	20LA	CE A 20 km, LLO, LAO
2 XG	4020A	CE A 40 km, CE B 20 km, LAO
	40LET	CE A 40 km, LLO, ET
	20LET	CE A 20 km, LLO, ET
3 XG	4020ET	CE A 40 km, CE B 20 km, ET

Table III. We consider four classes of networks containing, zero to three next-generation (XG) observatories. Each network is given a name to facilitate comparisons. The HLA network sets the stage, representing the baseline from which CE return on investment can be assessed. 40LA and 20LA represent a single CE operating in the context of an upgraded 2G network. 4020A is the CE reference configuration, operating with an upgraded LIGO Aundh, while 40LET and 20LET represent a single CE operating with LLO and ET. 4020ET is the reference CE configuration operating with ET.

is possible in the current facilities, we model the LIGO detectors in an upgraded form (known as “A<sup>#</sup>”, and essentially equivalent in sensitivity to “Voyager” [3]) that approximately represents the limit to what is achievable in the LIGO facilities. Furthermore, in addition to the LIGO Hanford (LHO) and LIGO Livingston (LLO) detectors, we also consider LIGO Aundh (LAO), as it is expected to be operational starting in the early 2030s. The strain sensitivity of A<sup>#</sup> is shown in Fig. 1.

c. *Einstein Telescope (ET)* The Einstein Telescope is a planned next-generation gravitational-wave observatory in Europe [4]. It is currently envisioned as an underground triangular facility with 10 km arm length, housing six interferometers. The targeted timeline calls for first observations by the mid-2030s. The underground location, which is imperative in Europe, suppresses the expected seismic disturbances, thereby reducing the Newtonian noise that limits ground-based gravitational-wave facilities a low frequencies (c.f. the difference between CE and ET below 8 Hz is depicted in Fig. 1).

ET’s adoption into the European Strategy Forum on Research Infrastructure (ESFRI) road map has affirmed the observatory’s role in the future of gravitational-wave physics astronomy. Nevertheless, we present network configurations that do not include ET to inform the value of US investment in the absence of ET. Our models for each of these network nodes are described below and shown in Table III.

## III. POPULATION OF COMPACT BINARIES

### A. Binary black holes

To analyze the science capabilities of the different detector network configurations, we construct populations

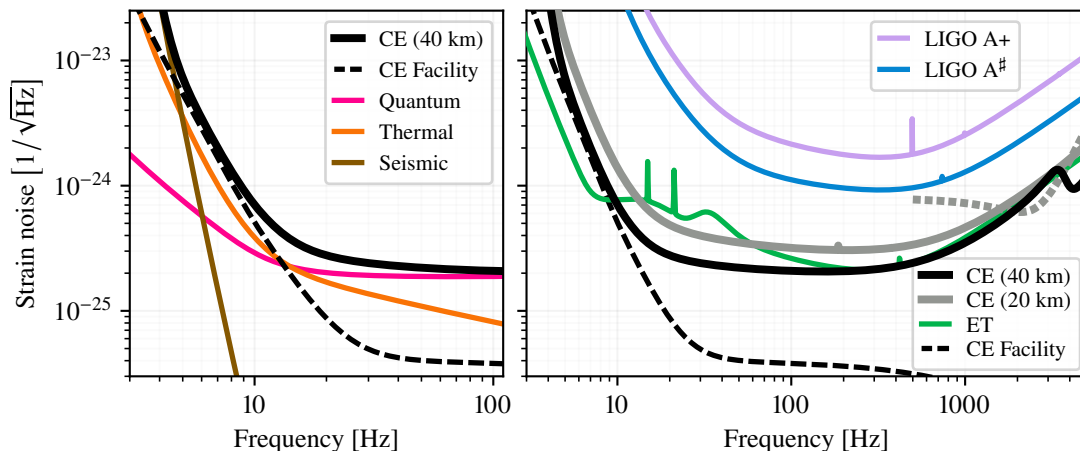


Figure 1. *Left*: Estimated spectral sensitivity (solid black) of Cosmic Explorer (CE) and the known fundamental sources of noise that contribute to this total (other curves). *Right*: Comparison of spectral sensitivities of LIGO A+, LIGO A<sup>#</sup>, Einstein Telescope (a triangular arrangement of six interferometric detectors), and 20 km and 40 km versions of Cosmic Explorer. The facility limit for Cosmic Explorer is also indicated. (From the Cosmic Explorer Horizon Study [2]).

of various types of compact binary mergers and evaluate the detection and measurement abilities of the networks for these populations. There are still large uncertainties in the properties that characterize these populations due to the low number of detections. While we attempt to choose populations that offer a fair representation of reality, we must also emphasize that the motive of this work is not to predict the actual detection rates but, instead, to compare the capabilities of different networks for the chosen populations.

### 1. Local population

The local population of BBH mergers closely resembles the population that has been inferred up to GWTC-3 [5, 6]. One difference is that we do not consider precession for any of the populations. As precession, in general, is expected to improve the estimation of parameters [cite], the measurability estimates presented in this work will be on the conservative side.

Specifically, for the local populations we use:

- **Primary mass:** POWER+PEAK [6] with the following true value of parameters:  $\alpha = -3.4$ ,  $m_{min} = 5 M_{\odot}$ ,  $m_{max} = 87 M_{\odot}$ ,  $\lambda = 0.04$ ,  $\mu_{peak} = 34 M_{\odot}$ ,  $\sigma_{peak} = 3.6$ ,  $\delta_m = 4.8 M_{\odot}$
- **Mass ratio:**  $p(q) \propto q^{\beta}$  with  $\beta = 1.1$ , and enforcing  $m_{min} = 5 M_{\odot}$
- **Spin magnitude:** Independently and identically distributed (IID) spins following a beta distribution with  $\alpha_{\chi} = 2$ ,  $\beta_{\chi} = 5$ , but restricted to aligned spins
- **Redshift:** Merger rate following the Madau-Dickinson star formation rate [7]. Using the same variables names of `gwpopulation`, we use  $\gamma_z = 2.7$ ,

$z_{peak} = 1.9$ ,  $\kappa = 5.6$ . We choose a local merger rate density of  $24 \text{ Gpc}^{-3} \text{ yr}^{-1}$

- **Waveform:** IMRPhenomXHM [8]

### 2. Population III black holes

We also consider a population of high-redshift BBHs, which might represent black holes remnants of Pop-III stars. As no uncontroversial detection of these objects exists, the uncertainty on their parameters is substantial. We use:

- **Primary mass:** A fixed value of  $20 M_{\odot}$
- **Mass ratio:** A fixed value of 0.9
- **Spin magnitude:** LVK's beta IIDs beta distributions with  $\alpha_{\chi} = 2$ ,  $\beta_{\chi} = 5$  (only considering aligned spins)
- **Redshift:** The merger rate follows the distribution introduced in Ref. [9] (Eq. C15) with  $a_{III} = 0.66$ ,  $b_{III} = 0.3$  and  $z_{III} = 11.6$
- **Waveform:** IMRPhenomXHM

### 3. Primordial black holes

In addition, we consider a population of even higher redshift sources, that could be representative of primordial black holes. For these too, our knowledge is limited. We use:

- **Primary and secondary mass:** The lognormal distribution of Ref. [10] (Eq. 1) centered at  $M_c = 30 M_{\odot}$  and with  $\sigma = 0.3 M_{\odot}$

- **Spin magnitude:** Zero spins
- **Redshift:** Merger rate distribution that increases as the age of the universe decreases (Ref. [10], Eq. 5).
- **Waveform:** IMRPhenomXHM

#### 4. Intermediate mass binary black holes (IMBBHs)

We would also like to know how well the next generation of GW observatories can characterize a population of intermediate-mass binary black hole (IMBBHs) binaries, especially with the improved sensitivity at low frequencies. We use:

- **Masses:** A power-law distribution for the two masses with  $\alpha = -2.5$ . Further, we choose  $m_{\min} = 100 M_{\odot}$  and  $m_{\max} = 1000 M_{\odot}$ .
- **Spins:** The spins for both the BHs are chosen to follow a uniform distribution between  $[-0.9, 0.9]$ .
- **Redshift:** A Madau-Dickinson-like merger rate, with  $\gamma_z = 2.7$ ,  $z_{\text{peak}} = 1.9$ ,  $\kappa = 5.6$ ; just as for the local BBHs. We choose a local merger rate density of  $1 \text{ Gpc}^{-3} \text{ yr}^{-1}$ .
- **Waveform:** IMRPhenomXHM

While the prescriptions above fix the characteristics for each formation channel, for Pop III and primordial black holes, we need two more parameters to fix the relative importance of these channels. We follow Refs. [9] and [10] and work with  $N_{\text{III}} = 2400$  and  $N_{\text{pbh}} = 600$  mergers per year in the two channels.

#### B. Binary neutron stars

We simulate a single population of BNSs, whose merger rate peaks at cosmic noon, and is consistent with the local merger rate as measured by the LVK. We choose the following parameters:

- **Primary and secondary mass:** A double Gaussian distribution,  $p(m) = w\mathcal{N}(\mu_L, \sigma_L) + (1 - w)\mathcal{N}(\mu_R, \sigma_R)$ . We use parameters equal to the median values of Ref. [11]:  $\mu_L = 1.35 M_{\odot}$ ,  $\sigma_L = 0.08 M_{\odot}$ ,  $\mu_R = 1.8 M_{\odot}$ ,  $\sigma_R = 0.3 M_{\odot}$ . Each normal distribution is independently truncated and normalized in the range  $[1, 2.2] M_{\odot}$ .
- **Spin magnitude:** Uniform in the range  $[0, 0.1]$
- **Redshift:** Same as local BBHs, but with a local merger rate density of  $320 \text{ Gpc}^{-3} \text{ yr}^{-1}$ .
- **Equation of state:** We use APR4 as the equation of state of the neutron star. Note that the maximum mass of the NS listed above corresponds to the maximum mass allowed by the APR4.

- **Waveform:** IMRPhenomPv2\_NRTidalv2 [cite]

While there is some evidence that the gravitational-wave source population differs from the galactic neutron-star population from which this bimodal mass distribution is derived, simulating a structured mass distribution allows us to verify if and how precisely the population can be characterized by next-generation detectors.

#### C. Neutron star-black hole mergers

Due to low number of detections, the properties of NSBH mergers are not well known. Because of this uncertainty, we will adopt a semi-agnostic approach to define the population for NSBH mergers. The specifications are as follows:

- **Black Hole Mass:** The POWER+PEAK distribution, same as primary mass of the BH.
- **Neutron Star Mass:** Uniform between  $[1, 2.2] M_{\odot}$ .
- **Spins:** For the BH, the spin is assumed to be aligned with the orbital angular momentum and follows a Gaussian distribution with  $\mu = 0$  and  $\sigma = 0.2$ . The NS is assumed to be slowly spinning, following a uniform distribution between  $[-0.1, 0.1]$ .
- **Redshift:** a Madau-Dickinson-like merger rate, with  $\gamma_z = 2.7$ ,  $z_{\text{peak}} = 1.9$ ,  $\kappa = 5.6$ ; just as for the local BBHs. We choose a local merger rate density of  $45 \text{ Gpc}^{-3} \text{ yr}^{-1}$ .
- **Waveform:** IMRPhenomXHM

For all other CBC parameters for all the cases (i.e. sky location, orbital orientation, polarization angle, coalescence time and phase) we use uninformative distributions. We assume all sources are quasi-circular, i.e. we ignore orbital eccentricity.

#### IV. DETECTION AND PARAMETER ESTIMATION OF THE POPULATIONS

Having introduced different network configurations and the populations models, we next wish to address the detectability of these sources classes and how precisely the parameters of these sources can be extracted with different detector configurations. Detectability is quantified in terms of matched filter signal to noise ratio  $\rho$  defined as

$$\rho^2 = 4 \int_{f_{\text{low}}}^{f_{\text{upper}}} \frac{|\tilde{h}_A|^2}{S_n^A} df, \quad (1)$$

where  $\tilde{h}_A$  is the waveform of the signal at detector A,  $S_n^A$  is the noise power spectral density (PSD) of detector A

and  $f_{\text{low}}$  and  $f_{\text{upper}}$  denote the lower and upper cut of frequencies of the integration.

Similarly, we use Fisher information matrix for computing the statistical uncertainties associated with the measurement of binary parameters. Fisher matrix  $\Gamma_{ab}$  is related to the derivatives of the waveform with respect to the set of source parameters  $\theta$  as

$$\Gamma_{ab} = 2 \int_{f_{\text{low}}}^{f_{\text{upper}}} \frac{\tilde{h}_{A,a} \tilde{h}_{A,b}^* + \tilde{h}_{A,a}^* \tilde{h}_{A,b}}{S_n^A} df, \quad (2)$$

where  $\star$  denotes the operation of complex conjugation. The inverse of Fisher matrix is called covariance matrix  $\Sigma_{ab}$  and the square root of the diagonal entries of it provides the  $1\sigma$  (68% CL) uncertainty range for the measurement of different parameters for a given detector A

$$\sigma_a = \sqrt{\Sigma_{aa}} \quad (3)$$

All measurement uncertainties mentioned here are at 68% credibility except that of angular resolution  $\Delta\Omega$  which reported at 90% credibility.

#### A. Detection efficiency and detection rate

Table IV. The reach corresponding to BBH events for the eight detector networks for the cases when the threshold SNR  $\rho_* = 10$  and  $\rho_* = 100$ .

Network	$\rho_* = 10$	$\rho_* = 100$
HLA	0.92	0.083
HLET	6.3	0.3
20LA	5.6	0.28
40LA	15	0.47
20LET	12	0.43
40LET	22	0.60
4020A	20	0.56
4020ET	27	0.67

Table V. The cosmic merger rate per year and the number of BBH events that are detected every year with SNRs greater than 10, 30, and 100 for the eight detector networks. The lower and upper bounds in the reported numbers are calculated using the uncertainty in the local merger rate density for BBH mergers.

Cosmic Rate	$9.6_{-2.8}^{+5.7} \times 10^4 \text{ yr}^{-1}$		
SNR $\rho$	> 10	> 30	> 100
HLA	$1.6_{-0.5}^{+9.3} \times 10^4$	$1.1_{-0.3}^{+6.3} \times 10^3$	$1.7_{-0.5}^{+1.2} \times 10^1$
HLET	$7.7_{-2.2}^{+4.5} \times 10^4$	$2.3_{-0.7}^{+1.3} \times 10^4$	$1.6_{-0.5}^{+9.0} \times 10^3$
20LA	$7.1_{-2.1}^{+4.1} \times 10^4$	$2.1_{-0.6}^{+1.2} \times 10^4$	$1.3_{-0.4}^{+7.3} \times 10^3$
40LA	$8.5_{-2.5}^{+4.9} \times 10^4$	$4.3_{-1.2}^{+2.5} \times 10^4$	$5.0_{-1.5}^{+3.0} \times 10^3$
20LET	$8.9_{-2.6}^{+5.2} \times 10^4$	$3.8_{-1.1}^{+2.3} \times 10^4$	$3.3_{-1.0}^{+2.0} \times 10^3$
40LET	$9.2_{-2.7}^{+5.4} \times 10^4$	$5.5_{-1.6}^{+3.2} \times 10^4$	$7.3_{-2.2}^{+4.3} \times 10^3$
4020A	$9.1_{-2.7}^{+5.3} \times 10^4$	$5.1_{-1.5}^{+3.0} \times 10^4$	$6.9_{-2.0}^{+4.0} \times 10^3$
4020ET	$9.5_{-2.8}^{+5.5} \times 10^4$	$6.1_{-1.8}^{+3.6} \times 10^4$	$9.2_{-2.7}^{+5.4} \times 10^3$

Table VI. The reach corresponding to BNS events for the eight detector networks for the cases when the threshold SNR  $\rho_* = 10$  and  $\rho_* = 100$ .

Network	$\rho_* = 10$	$\rho_* = 100$
HLA	0.18	0.018
HLET	0.66	0.062
20LA	0.61	0.058
40LA	1.1	0.096
20LET	1	0.089
40LET	1.4	0.12
4020A	1.3	0.11
4020ET	1.7	0.13

Table VII. The cosmic merger rate per year and the number of BNS events that are detected every year with SNRs greater than 10, 30, and 100 for the eight detector networks. The lower and upper bounds in the reported numbers are calculated using the uncertainty in the local merger rate density for BNS mergers.

Cosmic Rate	$1.2_{-0.9}^{+2.0} \times 10^6 \text{ yr}^{-1}$		
SNR $\rho$	> 10	> 30	> 100
HLA	$1.3_{-1.0}^{+1.9} \times 10^3$	$2.7_{-2.3}^{+6.6} \times 10^1$	0
HLET	$8.5_{-6.4}^{+13.0} \times 10^4$	$2.5_{-1.9}^{+3.9} \times 10^3$	$4.8_{-3.7}^{+7.4} \times 10^1$
20LA	$7.1_{-5.4}^{+11.0} \times 10^4$	$2.1_{-1.6}^{+3.1} \times 10^3$	$3.9_{-3.3}^{+6.7} \times 10^1$
40LA	$2.7_{-2.0}^{+4.1} \times 10^5$	$1.1_{-0.8}^{+1.7} \times 10^4$	$2.2_{-1.8}^{+3.3} \times 10^2$
20LET	$1.9_{-1.4}^{+2.9} \times 10^5$	$5.9_{-4.4}^{+9.0} \times 10^3$	$1.2_{-1.0}^{+1.9} \times 10^2$
40LET	$3.9_{-2.9}^{+5.9} \times 10^5$	$1.7_{-1.2}^{+2.6} \times 10^4$	$3.5_{-2.9}^{+5.5} \times 10^2$
4020A	$3.6_{-2.7}^{+5.5} \times 10^5$	$1.7_{-1.3}^{+2.6} \times 10^4$	$3.5_{-2.9}^{+5.6} \times 10^2$
4020ET	$4.7_{-3.5}^{+7.2} \times 10^5$	$2.3_{-1.8}^{+3.6} \times 10^4$	$4.8_{-3.9}^{+7.7} \times 10^2$

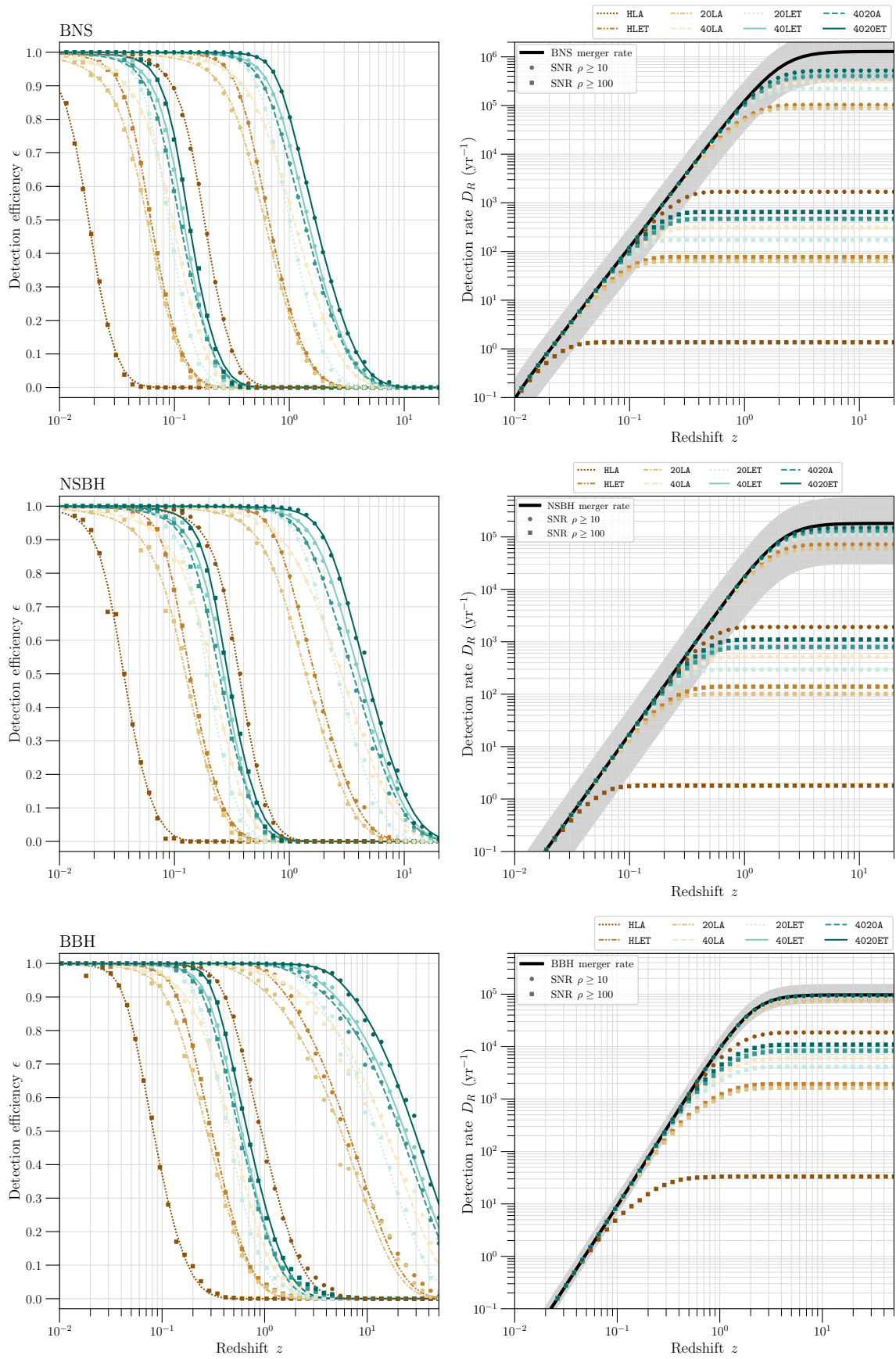


Figure 2. *Left panels:* The network efficiency curves for the eight gravitational-wave (GW) detector networks. The markers represent the efficiency at corresponding redshift values, and the lines are the *best-fit* sigmoid functions for the efficiency curves. *Right panels:* The detection rate as a function of redshift for the detector networks. The black solid line refers to the total merger rate. The gray shaded area shows the variation in the total merger rate due to the uncertainty in the value of the local merger rate density. From top to bottom the panels correspond to BNS, NSBH and BBH systems.

Table VIII. The reach corresponding to NSBH events for the eight detector networks for the cases when the threshold SNR  $\rho_* = 10$  and  $\rho_* = 100$ .

Network	$\rho_* = 10$	$\rho_* = 100$
HLA	0.36	0.036
HLET	1.5	0.13
20LA	1.4	0.12
40LA	2.8	0.21
20LET	2.5	0.19
40LET	3.8	0.26
4020A	3.5	0.24
4020ET	4.5	0.28

Table IX. The cosmic merger rate per year and the number of NSBH events that are detected every year with SNRs greater than 10, 30, and 100 for the eight detector networks. The lower and upper bounds in the reported numbers are calculated using the uncertainty in the local merger rate density for NSBH mergers.

Cosmic Rate	$1.8^{+3.8}_{-1.5} \times 10^5 \text{ yr}^{-1}$		
SNR $\rho$	> 10	> 30	> 100
HLA	$1.5^{+3.1}_{-1.2} \times 10^3$	$3.6^{+9.2}_{-3.3} \times 10^1$	$0.0^{+1.0}_{-0.0} \times 10^0$
HLET	$5.9^{+12.4}_{-4.8} \times 10^4$	$3.7^{+8.2}_{-3.1} \times 10^3$	$8.4^{+17.2}_{-7.2} \times 10^1$
20LA	$5.3^{+11.3}_{-4.4} \times 10^4$	$3.2^{+7.1}_{-2.7} \times 10^3$	$7.4^{+14.6}_{-6.7} \times 10^1$
40LA	$1.0^{+2.2}_{-0.9} \times 10^5$	$1.5^{+3.3}_{-1.3} \times 10^4$	$3.9^{+8.0}_{-3.2} \times 10^2$
20LET	$9.8^{+20.7}_{-8.1} \times 10^4$	$8.8^{+19.1}_{-7.3} \times 10^3$	$2.2^{+4.3}_{-1.8} \times 10^2$
40LET	$1.3^{+2.7}_{-1.1} \times 10^5$	$2.2^{+4.7}_{-1.8} \times 10^4$	$6.1^{+12.0}_{-5.1} \times 10^2$
4020A	$1.2^{+2.6}_{-1.0} \times 10^5$	$2.2^{+4.6}_{-1.8} \times 10^4$	$6.1^{+12.3}_{-5.1} \times 10^2$
4020ET	$1.4^{+3.0}_{-1.2} \times 10^5$	$2.9^{+6.2}_{-2.4} \times 10^4$	$8.4^{+17.1}_{-7.1} \times 10^2$

## B. Measurement uncertainty of source parameters

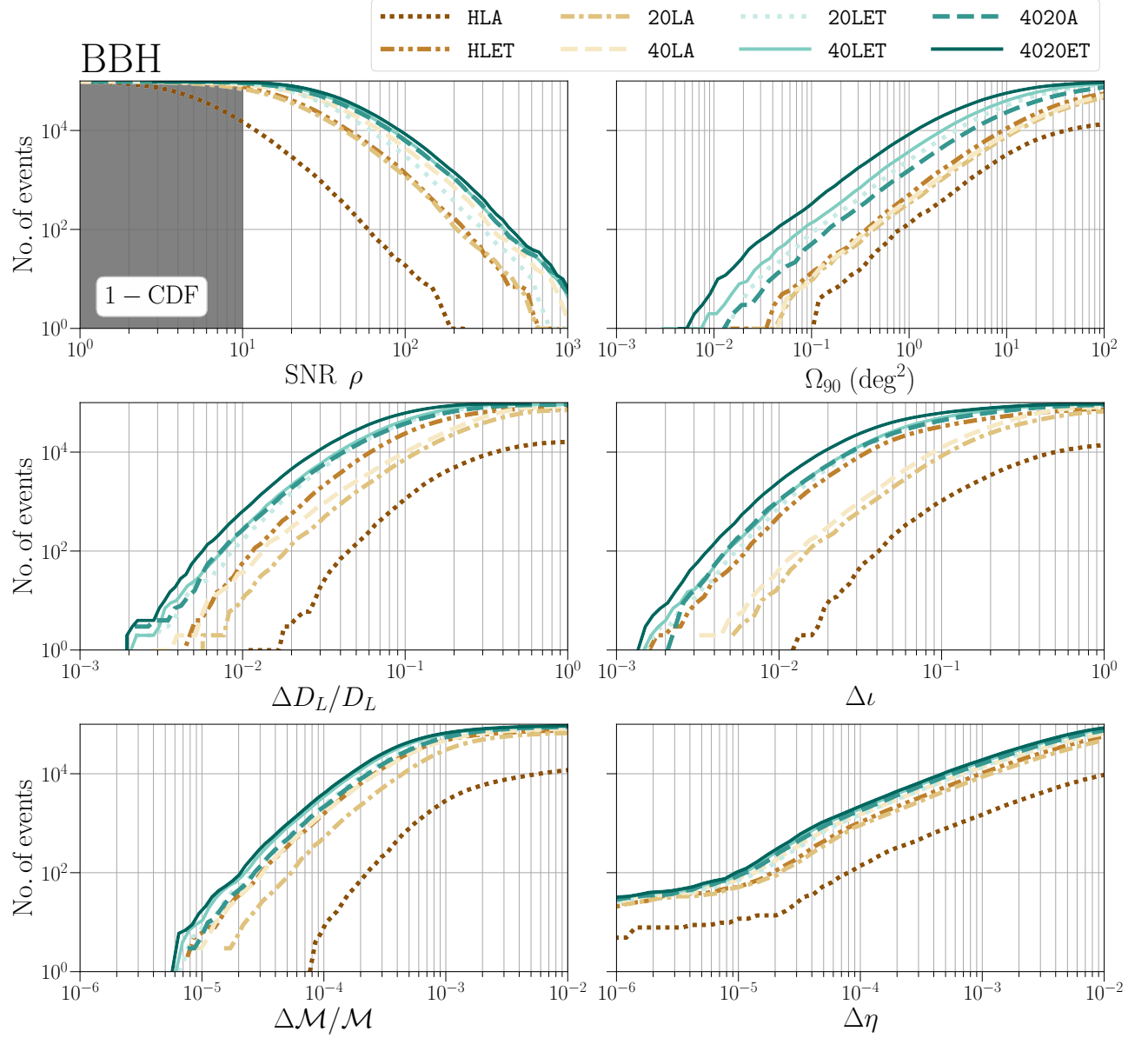


Figure 3. The scaled cumulative density function plots showing the trends in SNR  $\rho$  and sky-localization  $\Omega_{90}$  of the detected BBH events. It also shows the plots for fractional errors in chirp mass and luminosity distance, i.e.,  $\Delta \mathcal{M}/\mathcal{M}$  and  $\Delta D_L/D_L$ , and absolute errors in inclination angle, and symmetric mass ratio, i.e.,  $\Delta \iota$  and  $\Delta \eta$ , respectively.

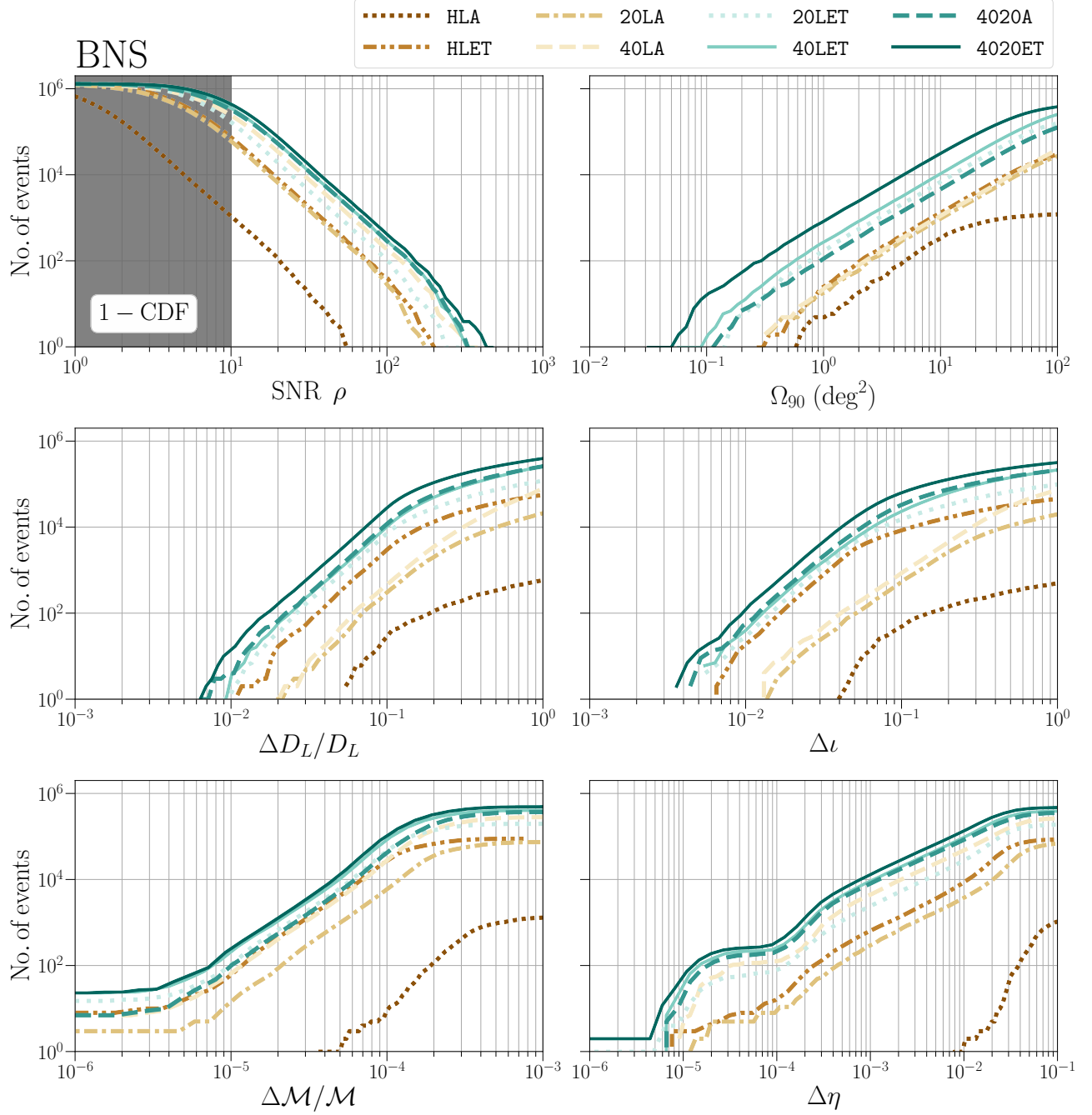


Figure 4. The scaled cumulative density function plots showing the trends in SNR  $\rho$  and sky-localization  $\Omega_{90}$  of the detected BNS events. It also shows the plots for fractional errors in chirp mass and luminosity distance, i.e.,  $\Delta\mathcal{M}/\mathcal{M}$  and  $\Delta D_L/D_L$ , and absolute errors in inclination angle, and symmetric mass ratio, i.e.,  $\Delta\iota$  and  $\Delta\eta$ , respectively.

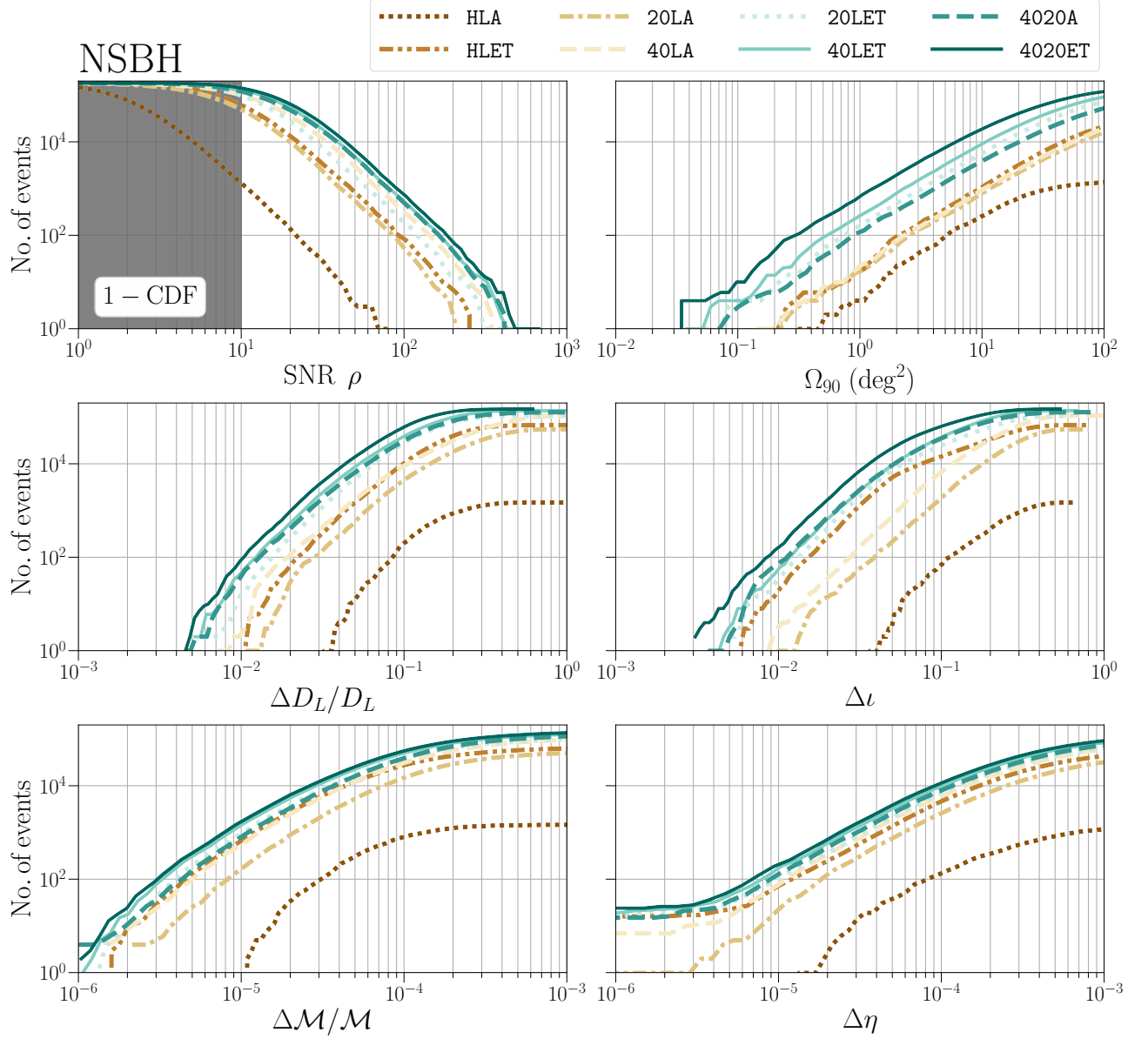


Figure 5. The scaled cumulative density function plots showing the trends in SNR  $\rho$  and sky-localization  $\Omega_{90}$  of the detected NSBH events. It also shows the plots for fractional errors in chirp mass and luminosity distance, i.e.,  $\Delta\mathcal{M}/\mathcal{M}$  and  $\Delta D_L/D_L$ , and absolute errors in inclination angle, symmetric mass ratio, and spins of the BH and the NS i.e.,  $\Delta\iota$ , and  $\Delta\eta$ , respectively.

Table X. The field of view (FOV) of some of the electromagnetic (EM) telescopes. The space telescopes in the list have been *italicized*.

Telescope	FOV (deg <sup>2</sup> )
Rubin [12, 13]	9.6
<i>EUCLID</i> [14]	0.54
<i>Athena</i> [15]	0.35
<i>Roman</i> [16, 17]	0.28
ngVLA [18] (2.4 GHz; FWHM)	0.17
<i>Chandra X-ray</i> [19]	0.15
<i>Lynx</i> [20]	0.13
<i>Swift-XRT</i> [21]	0.12
Keck [22]	0.11
Jansky VLA [23] (3 GHz; FWHM)	0.0625

### C. 3D localization of sources

In addition to the source parameters, one can also infer the sky location and the luminosity distance associated with the source from the GW data. Precise localization of the source is critical for multiple science objectives. Assuming that the cosmology is known, accurate distance estimation enables the calculation of source-frame masses of the binary objects, which are important for unraveling the mass spectrum and distinguishing between formation channels (see section V A). Localization of the source plays a crucial role in enabling multimessenger astronomy (MMA) (see section V B) and inference of cosmological parameters (see section V D). The localization of the source from GW observations is communicated to electromagnetic (EM) telescopes, which allows them to capture EM transients that may follow the binary merger. While the field of view (FOV) of EM telescopes is, in general, smaller than 10 deg<sup>2</sup> (see Table X), they can cover multiple patches in the sky to observe large sky areas. Thus, precise localization and timely communication are necessary to facilitate MMA.

Table XI shows the number of BBH detections every year for varying precision of sky-localization and luminosity distance measurement. Without any XG detectors, a network with three A<sup>#</sup> detectors is only able to localize  $\sim 1\%$  of all BBH mergers to a smaller area than 100 deg<sup>2</sup> in the sky. Having just one XG detector enhances this fraction to  $\sim 50\%$ , whereas a network with three XG detectors is able to localize  $\sim 95\%$  of all BBH mergers to  $\Delta\Omega \leq 100$  deg<sup>2</sup>. Further, networks with at least two XG detectors localize  $\mathcal{O}(1000)$  BBH events every year to better than 1 deg<sup>2</sup>, which is an order of magnitude more events compared to if the network contains only one XG detector. In addition, fig. 6 also shows that only networks with at least two XG detectors are able to localize events to  $\Delta\Omega \leq 0.1$  deg<sup>2</sup>. This metric is of particular

relevance to host-galaxy identification, as the number of galaxies lying within an observation volume scale linearly with sky area.

The luminosity distance measurement is also aided by the improved sensitivity of the XG detectors. For a network with three A<sup>#</sup> detectors, we can expect about 100 BBH mergers every year for which the error in luminosity distance is within 10%. However,  $D_L$  cannot be measured to 1% precision for any of the events. For networks with two or more XG detectors, not only will they detect thousands of BBH mergers every year for which  $\Delta D_L/D_L \leq 0.1$ , but they will also detect tens of events for which  $D_L$  is measured to sub-percent precision.

Table XI. The number of BBH detections per year for the six detector networks with 90%-credible sky area less than 10, 1, 0.1 and 0.01 deg<sup>2</sup> and fractional error in luminosity distance less than 0.1 and 0.01.

Metric	$\Omega_{90}$ (deg) <sup>2</sup>					$\Delta D_L/D_L$	
	$\leq 100$	$\leq 10$	$\leq 1$	$\leq 0.1$	$\leq 0.01$	$\leq 0.1$	$\leq 0.01$
HLA	$1.3^{+7.8}_{-0.4} \times 10^4$	$3.3^{+1.9}_{-1.0} \times 10^3$	$1.4^{+8.1}_{-0.5} \times 10^2$	$4.0^{+0.0}_{-1.0} \times 10^0$	0	$9.0^{+5.3}_{-2.6} \times 10^2$	0
HLET	$5.2^{+3.1}_{-1.5} \times 10^4$	$1.0^{+5.8}_{-0.3} \times 10^4$	$4.9^{+3.1}_{-1.4} \times 10^2$	$1.3^{+2.0}_{-0.4} \times 10^1$	0	$2.1^{+1.2}_{-0.6} \times 10^4$	$4.7^{+3.2}_{-1.1} \times 10^1$
20LA	$4.4^{+2.6}_{-1.3} \times 10^4$	$7.4^{+4.3}_{-2.1} \times 10^3$	$3.5^{+2.1}_{-1.0} \times 10^2$	$8.0^{+3.0}_{-3.0} \times 10^0$	0	$6.2^{+3.6}_{-1.8} \times 10^3$	$1.2^{+1.0}_{-0.4} \times 10^1$
40LA	$4.8^{+2.8}_{-1.4} \times 10^4$	$8.2^{+4.8}_{-2.4} \times 10^3$	$4.0^{+2.4}_{-1.1} \times 10^2$	$9.0^{+5.0}_{-3.0} \times 10^0$	0	$9.4^{+5.5}_{-2.8} \times 10^3$	$3.7^{+2.0}_{-1.2} \times 10^1$
20LET	$8.1^{+4.7}_{-2.5} \times 10^4$	$3.0^{+1.7}_{-0.9} \times 10^4$	$2.4^{+1.4}_{-0.7} \times 10^3$	$7.8^{+3.6}_{-2.8} \times 10^1$	$2.0^{+0.0}_{-0.0} \times 10^0$	$3.7^{+2.2}_{-1.1} \times 10^4$	$1.4^{+8.9}_{-0.4} \times 10^2$
40LET	$8.5^{+5.0}_{-2.5} \times 10^4$	$3.7^{+2.1}_{-1.1} \times 10^4$	$3.5^{+2.1}_{-1.1} \times 10^3$	$1.2^{+7.2}_{-0.4} \times 10^2$	$3.0^{+0.0}_{-1.0} \times 10^0$	$4.2^{+2.5}_{-1.2} \times 10^4$	$2.3^{+1.3}_{-0.7} \times 10^2$
4020A	$7.0^{+4.1}_{-2.0} \times 10^4$	$2.1^{+1.2}_{-0.6} \times 10^4$	$1.5^{+8.5}_{-0.5} \times 10^3$	$5.2^{+3.0}_{-1.4} \times 10^1$	$1.0^{+0.0}_{-0.0} \times 10^0$	$3.5^{+2.1}_{-1.0} \times 10^4$	$1.9^{+1.3}_{-0.5} \times 10^2$
4020ET	$9.1^{+5.3}_{-2.7} \times 10^4$	$5.2^{+3.1}_{-1.5} \times 10^4$	$7.6^{+4.5}_{-2.2} \times 10^3$	$3.4^{+2.0}_{-1.0} \times 10^2$	$7.0^{+2.0}_{-4.0} \times 10^0$	$6.0^{+3.5}_{-1.8} \times 10^4$	$5.3^{+3.1}_{-1.5} \times 10^2$

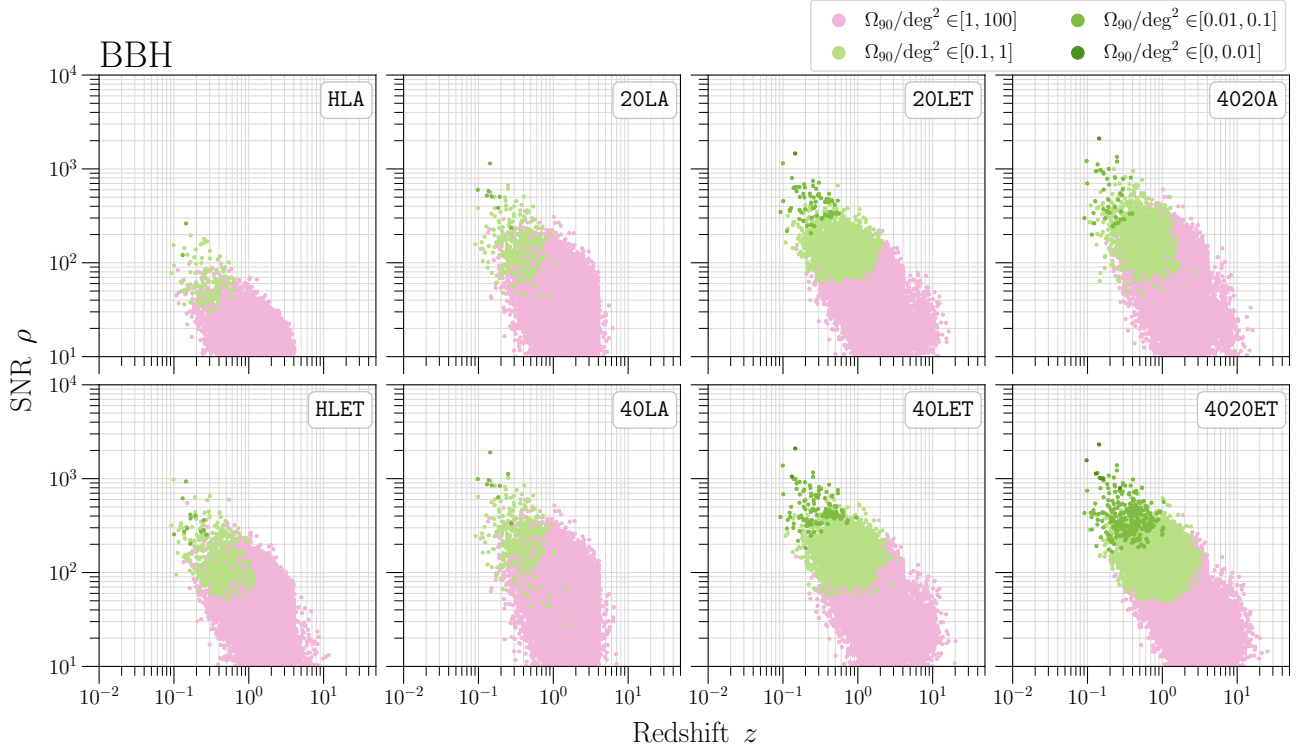


Figure 6. Plot showing the relationship between SNR  $\rho$ , sky localization  $\Omega_{90}$  and the redshift  $z$  for events belonging to the Pop-1 population, corresponding to the eight GW detector networks. Each marker is an event detected by the corresponding detector network in an observation time of 1 year. The color of the marker conveys how well that event can be localized in the sky using GW observation.

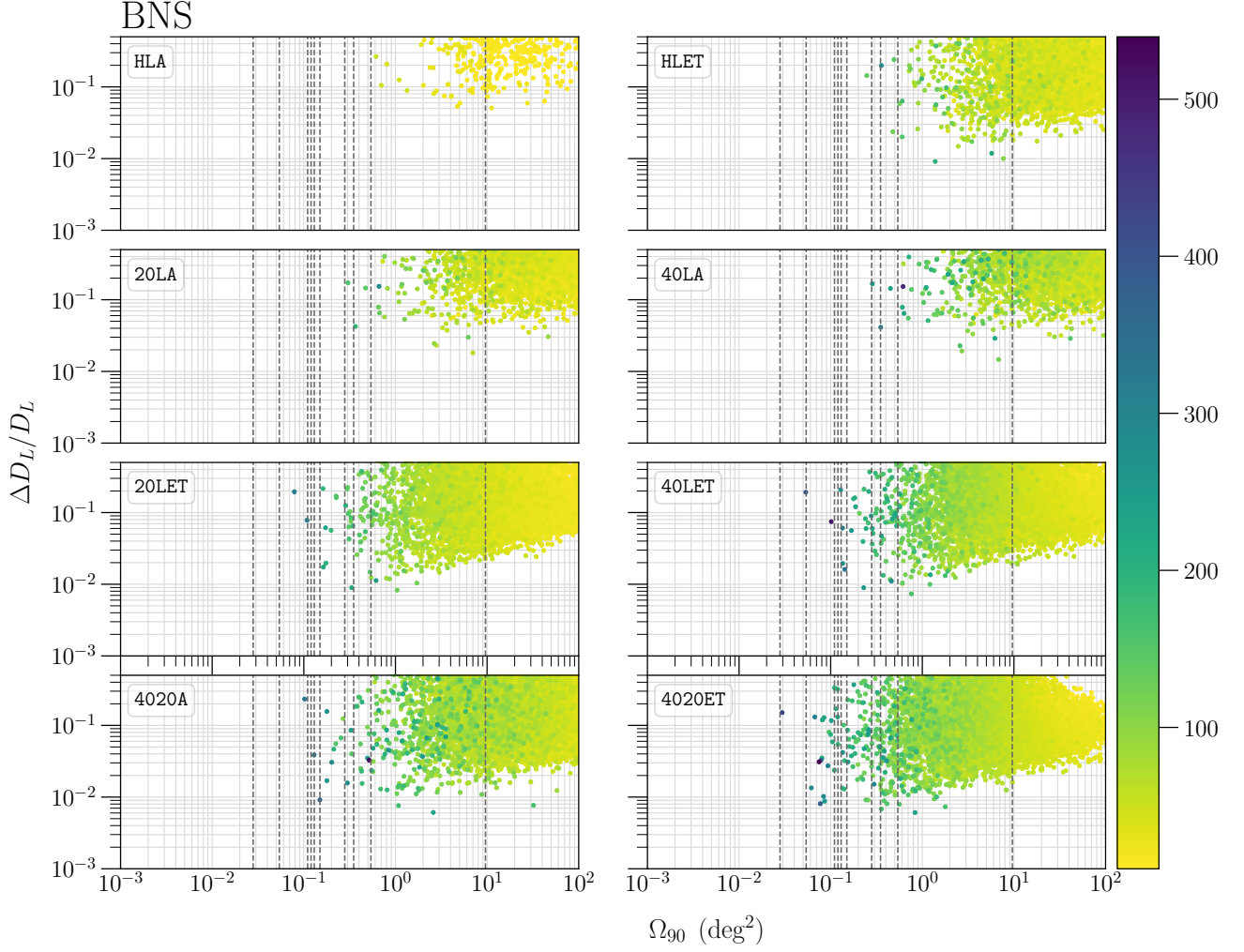


Figure 7. The figure shows the relationship between the fractional error in luminosity distance  $\Delta D_L/D_L$ , 90%-credible sky area  $\Omega_{90}$  and the SNR (denoted by the color bar) of BNS events for which  $z < 0.5$ . Each of these events, detected in an observation span of 1 year, appears as a spot placed according to the associated measurement errors in luminosity distance and sky position. The color of the dots represents the SNR with which that particular event was detected in a GW detector network.

Table XII. For the sub-population with BNS events for which  $z < 0.5$ , the table lists the number of detections per year for the six detector networks with 90%-credible sky area  $\Omega_{90} < 10, 1, 0.1$  and  $0.01 \text{ deg}^2$  and fractional error in luminosity distance  $\Delta D_L/D_L < 0.1$  and  $0.01$ .

Metric	$\Omega_{90} \text{ (deg}^2\text{)}$					$\Delta D_L/D_L$	
	$\leq 100$	$\leq 10$	$\leq 1$	$\leq 0.1$	$\leq 0.01$	$\leq 0.1$	$\leq 0.01$
HLA	$1.2^{+1.8}_{-0.9} \times 10^3$	$3.2^{+4.7}_{-2.5} \times 10^2$	$5.0^{+11.0}_{-5.0} \times 10^0$	0	0	$2.6^{+4.2}_{-2.3} \times 10^1$	0
HLET	$1.0^{+1.5}_{-0.8} \times 10^4$	$1.2^{+1.8}_{-0.9} \times 10^3$	$2.4^{+4.7}_{-2.1} \times 10^1$	$0.0^{+3.0}_{-0.0} \times 10^0$	0	$2.3^{+3.4}_{-1.7} \times 10^3$	$1.0^{+2.0}_{-1.0} \times 10^0$
20LA	$8.6^{+13.3}_{-6.4} \times 10^3$	$8.6^{+12.9}_{-6.8} \times 10^2$	$1.7^{+3.3}_{-1.5} \times 10^1$	0	0	$2.4^{+4.2}_{-1.9} \times 10^2$	0
40LA	$9.8^{+15.1}_{-7.3} \times 10^3$	$9.7^{+14.6}_{-7.6} \times 10^2$	$1.8^{+3.8}_{-1.6} \times 10^1$	0	0	$3.1^{+5.4}_{-2.4} \times 10^2$	$0.0^{+2.0}_{-0.0} \times 10^0$
20LET	$1.5^{+2.3}_{-1.1} \times 10^4$	$4.9^{+7.4}_{-3.7} \times 10^3$	$1.6^{+2.4}_{-1.3} \times 10^2$	$1.0^{+6.0}_{-1.0} \times 10^0$	0	$4.4^{+6.9}_{-3.3} \times 10^3$	$2.0^{+6.0}_{-2.0} \times 10^0$
40LET	$1.6^{+2.4}_{-1.2} \times 10^4$	$6.3^{+9.7}_{-4.8} \times 10^3$	$2.5^{+3.8}_{-2.0} \times 10^2$	$1.0^{+9.0}_{-1.0} \times 10^0$	0	$4.9^{+7.7}_{-3.7} \times 10^3$	$2.0^{+9.0}_{-2.0} \times 10^0$
4020A	$1.4^{+2.1}_{-1.0} \times 10^4$	$3.4^{+5.3}_{-2.6} \times 10^3$	$9.7^{+15.7}_{-7.7} \times 10^1$	$0.0^{+4.0}_{-0.0} \times 10^0$	0	$4.5^{+6.9}_{-3.4} \times 10^3$	$4.0^{+11.0}_{-4.0} \times 10^0$
4020ET	$1.6^{+2.5}_{-1.2} \times 10^4$	$1.0^{+1.5}_{-0.8} \times 10^4$	$7.5^{+11.4}_{-5.8} \times 10^2$	$1.3^{+2.9}_{-1.2} \times 10^1$	$0.0^{+2.0}_{-0.0} \times 10^0$	$8.5^{+13.1}_{-6.4} \times 10^3$	$1.2^{+2.2}_{-1.2} \times 10^1$

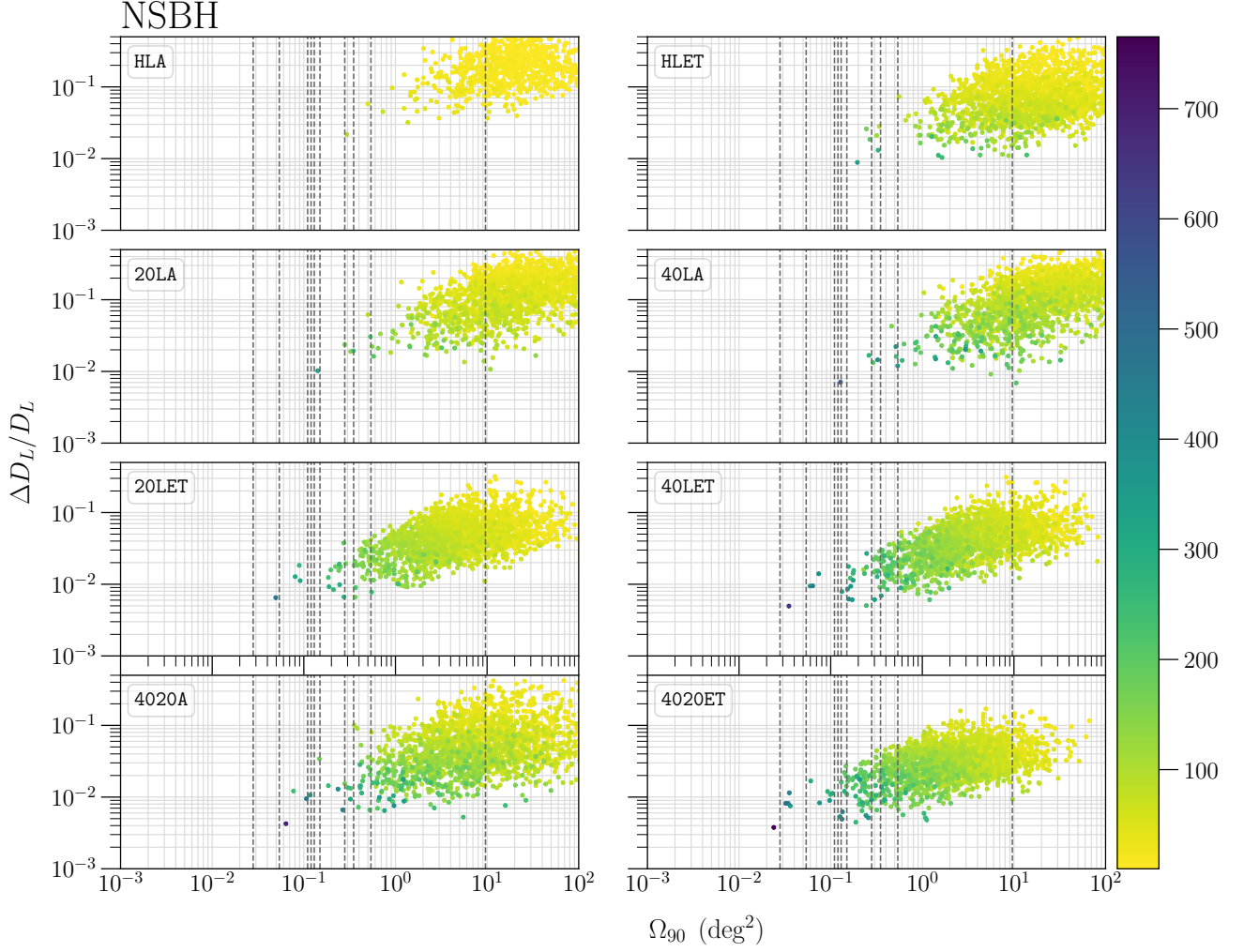


Figure 8. The figure shows the relationship between the fractional error in luminosity distance  $\Delta D_L/D_L$ , 90%-credible sky area  $\Omega_{90}$  and the SNR (denoted by the color bar) of NSBH events for which  $z < 0.5$ . Each of these events, detected in an observation span of 1 year, appears as a spot placed according to the associated measurement errors in luminosity distance and sky position. The color of the dots represents the SNR with which that particular event was detected in a GW detector network.

Table XIII. For the sub-population with events for which  $z < 0.5$ , the table lists the number of detections per year for the six detector networks with 90%-credible sky area  $\Omega_{90} < 10, 1, 0.1$  and  $0.01 \text{ deg}^2$  and fractional error in luminosity distance  $\Delta D_L/D_L < 0.1$  and  $0.01$ .

Metric	$\Omega_{90} \text{ (deg}^2\text{)}$					$\Delta D_L/D_L$	
	$\leq 100$	$\leq 10$	$\leq 1$	$\leq 0.1$	$\leq 0.01$	$\leq 0.1$	$\leq 0.01$
HLA	$9.3^{+19.9}_{-7.8} \times 10^2$	$2.6^{+4.9}_{-2.2} \times 10^2$	$6.0^{+17.0}_{-5.0} \times 10^0$	0	0	$1.5^{+3.4}_{-1.3} \times 10^2$	0
HLET	$2.0^{+4.3}_{-1.6} \times 10^3$	$6.8^{+14.8}_{-5.7} \times 10^2$	$2.3^{+5.6}_{-2.1} \times 10^1$	$0.0^{+2.0}_{-0.0} \times 10^0$	0	$1.5^{+3.2}_{-1.2} \times 10^3$	$3.0^{+18.0}_{-3.0} \times 10^0$
CE20LA	$1.9^{+4.1}_{-1.6} \times 10^3$	$5.3^{+11.4}_{-4.5} \times 10^2$	$1.7^{+2.9}_{-1.6} \times 10^1$	$0.0^{+1.0}_{-0.0} \times 10^0$	0	$7.3^{+15.8}_{-6.2} \times 10^2$	$2.0^{+9.0}_{-2.0} \times 10^0$
CE40LA	$1.9^{+4.2}_{-1.6} \times 10^3$	$5.8^{+12.5}_{-4.9} \times 10^2$	$2.0^{+3.9}_{-1.9} \times 10^1$	$0.0^{+1.0}_{-0.0} \times 10^0$	0	$9.6^{+20.6}_{-8.0} \times 10^2$	$9.0^{+23.0}_{-8.0} \times 10^0$
CE20LET	$2.3^{+4.9}_{-1.9} \times 10^3$	$1.6^{+3.4}_{-1.3} \times 10^3$	$1.5^{+3.1}_{-1.3} \times 10^2$	$3.0^{+7.0}_{-2.0} \times 10^0$	0	$2.0^{+4.4}_{-1.7} \times 10^3$	$2.1^{+5.3}_{-1.9} \times 10^1$
CE40LET	$2.3^{+4.9}_{-1.9} \times 10^3$	$1.8^{+3.8}_{-1.5} \times 10^3$	$2.6^{+5.0}_{-2.2} \times 10^2$	$5.0^{+12.0}_{-4.0} \times 10^0$	0	$2.1^{+4.6}_{-1.8} \times 10^3$	$5.1^{+10.2}_{-4.6} \times 10^1$
CE4020A	$2.2^{+4.7}_{-1.8} \times 10^3$	$1.2^{+2.7}_{-1.0} \times 10^3$	$9.4^{+18.4}_{-8.7} \times 10^1$	$0.0^{+10.0}_{-0.0} \times 10^0$	0	$1.9^{+3.9}_{-1.6} \times 10^3$	$4.5^{+7.8}_{-3.9} \times 10^1$
CE4020ET	$2.3^{+4.9}_{-1.9} \times 10^3$	$2.1^{+4.5}_{-1.7} \times 10^3$	$5.4^{+10.9}_{-4.6} \times 10^2$	$1.3^{+3.1}_{-1.2} \times 10^1$	$0.0^{+1.0}_{-0.0} \times 10^0$	$2.3^{+4.8}_{-1.9} \times 10^3$	$8.8^{+17.9}_{-7.7} \times 10^1$

Table XIV. The number of BNS detections per year for the GW detector networks for which an EW alert can be sent 60 s, 120 s, 300 s and 600 s before the merger, with 90%-credible sky area measured to be better than 100, 10, 1 deg<sup>2</sup> at the time when the alert is sent.

EW Time	$\tau_{\text{EW}} = 60 \text{ s}$			$\tau_{\text{EW}} = 120 \text{ s}$		
	$\leq 100$	$\leq 10$	$\leq 1$	$\leq 100$	$\leq 10$	$\leq 1$
$\Omega_{90} \text{ (deg}^2\text{)}$						
HLA	$0.0_{-0.0}^{+1.0} \times 10^0$	0	0	0	0	0
HLET	$1.3_{-1.1}^{+2.4} \times 10^2$	$1.0_{-1.0}^{+10.0} \times 10^0$	0	$8.3_{-6.9}^{+15.7} \times 10^1$	$1.0_{-1.0}^{+5.0} \times 10^0$	0
20LA	$5.0_{-4.0}^{+10.0} \times 10^0$	0	0	$2.0_{-1.0}^{+1.0} \times 10^0$	0	0
40LA	$7.0_{-6.0}^{+19.0} \times 10^0$	0	0	$3.0_{-2.0}^{+6.0} \times 10^0$	0	0
20LET	$2.0_{-1.6}^{+3.2} \times 10^3$	$4.9_{-4.0}^{+9.7} \times 10^1$	$1.0_{-1.0}^{+3.0} \times 10^0$	$1.2_{-0.9}^{+1.8} \times 10^3$	$3.0_{-2.4}^{+5.5} \times 10^1$	$0.0_{-0.0}^{+2.0} \times 10^0$
40LET	$3.4_{-2.6}^{+5.2} \times 10^3$	$1.2_{-0.9}^{+1.9} \times 10^2$	$2.0_{-2.0}^{+4.0} \times 10^0$	$2.3_{-1.7}^{+3.5} \times 10^3$	$7.4_{-6.3}^{+12.0} \times 10^1$	$1.0_{-1.0}^{+2.0} \times 10^0$
4020A	$3.7_{-2.8}^{+6.2} \times 10^2$	$1.5_{-1.2}^{+2.3} \times 10^1$	0	$2.2_{-1.7}^{+3.1} \times 10^2$	$1.1_{-0.9}^{+1.0} \times 10^1$	0
4020ET	$6.3_{-4.7}^{+9.4} \times 10^3$	$2.7_{-2.1}^{+4.5} \times 10^2$	$5.0_{-4.0}^{+12.0} \times 10^0$	$4.4_{-3.3}^{+6.6} \times 10^3$	$1.5_{-1.2}^{+2.6} \times 10^2$	$1.0_{-1.0}^{+4.0} \times 10^0$
EW Time	$\tau_{\text{EW}} = 300 \text{ s}$			$\tau_{\text{EW}} = 600 \text{ s}$		
	$\leq 100$	$\leq 10$	$\leq 1$	$\leq 100$	$\leq 10$	$\leq 1$
$\Omega_{90} \text{ (deg}^2\text{)}$						
HLA	0	0	0	0	0	0
HLET	$4.2_{-3.5}^{+7.9} \times 10^1$	$0.0_{-0.0}^{+2.0} \times 10^0$	0	$2.4_{-1.9}^{+4.3} \times 10^1$	$0.0_{-0.0}^{+1.0} \times 10^0$	0
20LA	0	0	0	0	0	0
40LA	0	0	0	0	0	0
CE20LET	$4.7_{-3.6}^{+7.6} \times 10^2$	$7.0_{-6.0}^{+26.0} \times 10^0$	0	$2.0_{-1.6}^{+3.2} \times 10^2$	$4.0_{-4.0}^{+11.0} \times 10^0$	0
40LET	$1.0_{-0.8}^{+15.9} \times 10^3$	$2.2_{-1.7}^{+53.0} \times 10^1$	$0.0_{-0.0}^{+1.0} \times 10^0$	$4.1_{-3.2}^{+6.7} \times 10^2$	$6.0_{-5.0}^{+22.0} \times 10^0$	0
4020A	$6.2_{-5.2}^{+8.5} \times 10^1$	$2.0_{-2.0}^{+0.0} \times 10^0$	0	$1.9_{-1.6}^{+2.0} \times 10^1$	0	0
4020ET	$1.8_{-1.4}^{+28.6} \times 10^3$	$5.2_{-4.3}^{+9.3} \times 10^1$	$0.0_{-0.0}^{+2.0} \times 10^0$	$6.8_{-5.3}^{+11.2} \times 10^2$	$1.5_{-1.2}^{+3.7} \times 10^1$	$0.0_{-0.0}^{+1.0} \times 10^0$

Table XV. # of BNS mergers every year corresponding to Table 2 (Science Goal Requirements) of the CE White Paper. These numbers were calculated using the median local merger rates for BNS ( $320 \text{ Gpc}^3 \text{ yr}^{-1}$ ).

Criteria	<b>0 XG</b>	<b>1 XG</b>		<b>2 XG</b>			<b>3 XG</b>	
	HLA	HLET	CE20LA	CE40LA	CE20LET	CE40LET	CE4020A	CE4020ET
# at $z \leq 0.06$ with $\Delta\Omega \leq 0.1 \text{ deg}^2$	0	0	0	0	1	1	0	7
# at $0.06 < z \leq 0.1$ with $\Delta\Omega \leq 1 \text{ deg}^2$	1	8	6	6	32	47	26	71
# at $0.1 < z \leq 2$ with $\Delta\Omega \leq 10 \text{ deg}^2$	257	1126	783	892	6111	9339	3907	27668
# at $z > 2$ with $\Delta\Omega \leq 100 \text{ deg}^2$	0	2	19	37	6342	24974	3729	65537
# at $z \geq 5$	0	0	02	8	0	336	570	870

Table XVI. # of BNS mergers every year corresponding to specific multimessenger needs. These numbers were calculated using the median local merger rates for BNS ( $320 \text{ Gpc}^3 \text{ yr}^{-1}$ ).

Criteria	<b>0 XG</b>	<b>1 XG</b>			<b>2 XG</b>			<b>3 XG</b>
	HLA	HLET	CE20LA	CE40LA	CE20LET	CE40LET	CE4020A	CE4020ET
$\Omega_{90} \leq 0.1 \text{ deg}^2$								
Number	0	0	0	0	1	1	0	13
Median $z$	---	---	---	---	0.052	0.052	---	0.056
Maximum $z$	---	---	---	---	0.052	0.052	---	0.129
$\Omega_{90} \leq 1 \text{ deg}^2$								
Number	5	24	17	18	157	247	97	754
Median $z$	0.056	0.090	0.072	0.082	0.102	0.128	0.108	0.185
Maximum $z$	0.101	0.156	0.126	0.126	0.230	0.287	0.243	0.503
$\Omega_{90} \leq 10 \text{ deg}^2$								
Number	317	1216	866	976	6211	9440	4004	27771
Median $z$	0.152	0.208	0.216	0.199	0.360	0.410	0.327	0.599
Maximum $z$	0.359	0.535	0.522	0.535	1.08	1.30	1.06	2.12
$\Omega_{90} \leq 100 \text{ deg}^2$								
Number	1206	28271	25148	34114	148626	235160	113998	362848
Median $z$	0.209	0.602	0.625	0.677	1.03	1.19	0.976	1.35
Maximum $z$	0.516	2.12	2.23	2.23	3.68	5.89	3.645	8.80
$\text{SNR} \geq 100$								
Number	0	48	39	220	123	351	353	480
Median $z$	---	0.099	0.105	0.136	0.112	0.142	0.147	0.152
Maximum $z$	---	0.171	0.166	0.282	0.215	0.329	0.367	0.367
Median $\Omega_{90} \text{ (deg}^2\text{)}$	---	2.35	2.70	4.13	0.617	0.858	1.99	0.578
Maximum $\Omega_{90} \text{ (deg}^2\text{)}$	---	9.71	9.98	50.5	3.01	4.64	43.30	2.99
$\text{SNR} \geq 300$								
Number	0	0	0	2	2	4	4	6
Median $z$	---	---	---	0.050	0.048	0.051	0.051	0.054
Maximum $z$	---	---	---	0.057	0.052	0.056	0.056	0.101
Median $\Omega_{90} \text{ (deg}^2\text{)}$	---	---	---	0.489	0.095	0.118	0.141	0.076
Maximum $\Omega_{90} \text{ (deg}^2\text{)}$	---	---	---	0.622	0.110	0.142	0.522	0.094

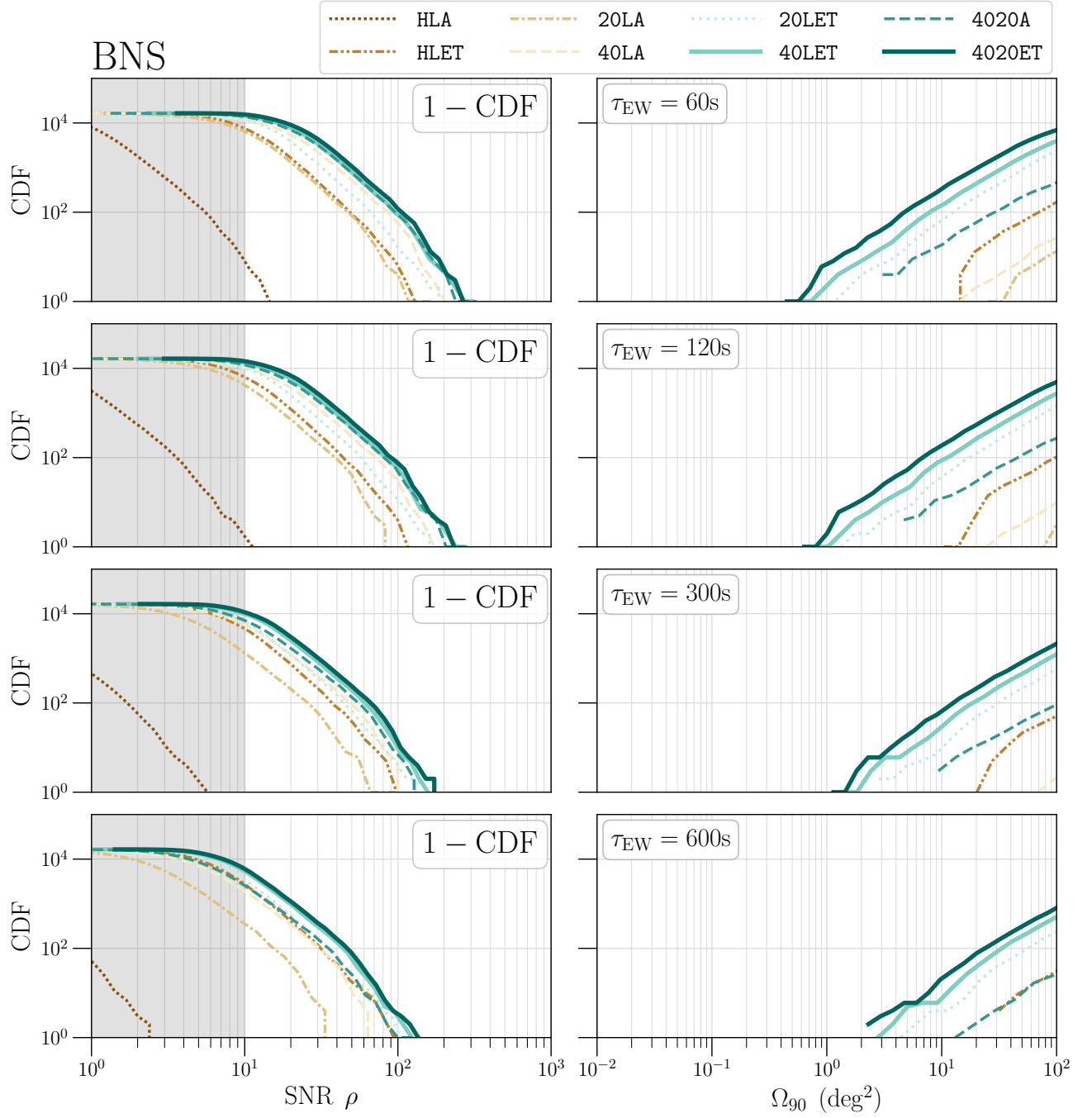


Figure 9. The scaled CDF plots for BNS events belonging to the multimessenger sub-population for which early-warning alerts can be sent 1 minute, 2 minutes, 5 minutes, and 10 minutes before their respective mergers.

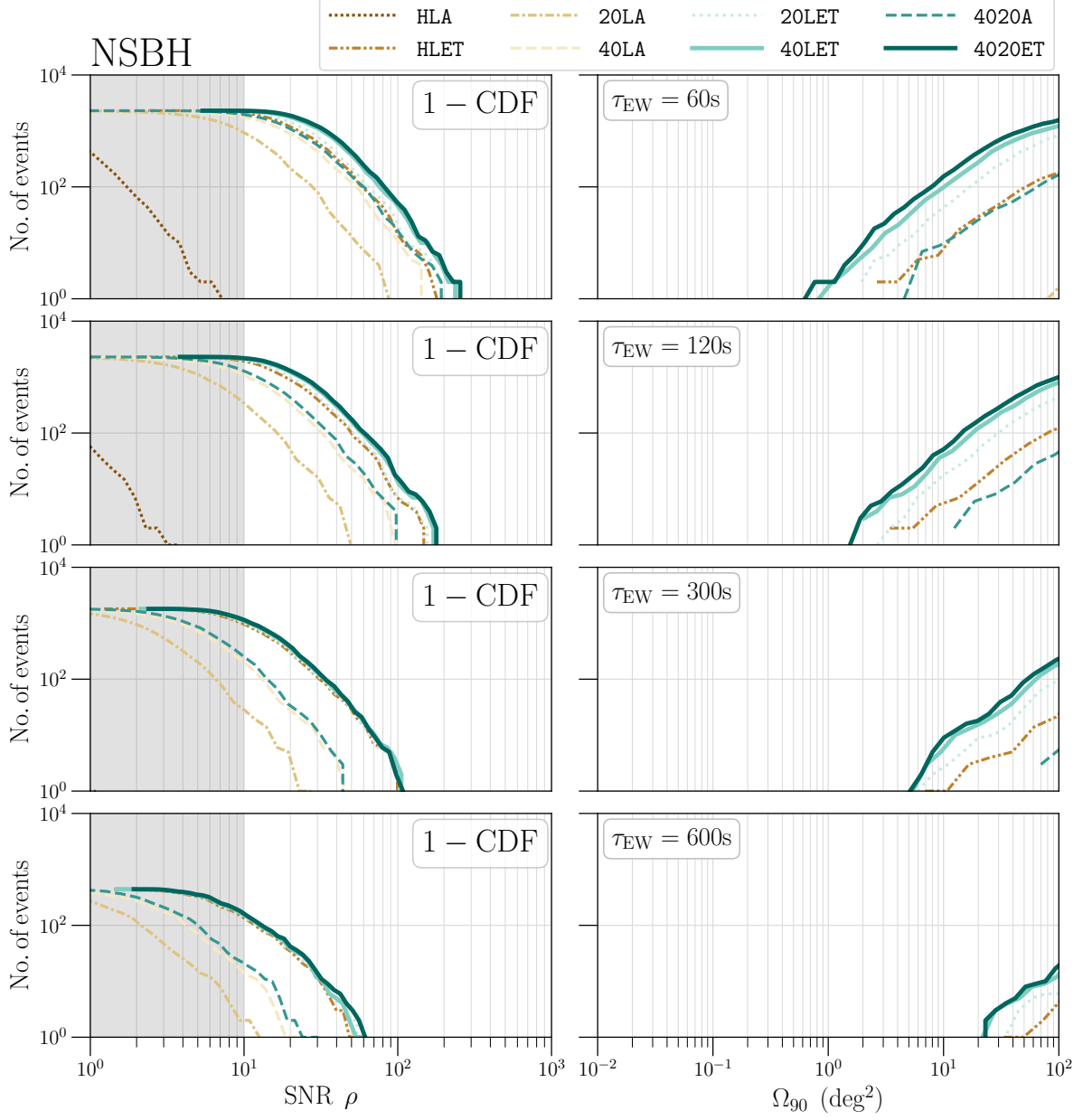


Figure 10. The scaled CDF plots for NSBH events belonging to the multimessenger sub-population for which early-warning alerts can be sent 1 minute, 2 minutes, 5 minutes, and 10 minutes before their respective mergers.

Table XVII. The number of detections per year for the GW detector networks for which an EW alert can be sent 60 s, 120 s, 300 s and 600 s before the merger, with 90%-credible sky area measured to be better than 100, 10, 1 deg<sup>2</sup> at the time when the alert is sent.

EW Time		$\tau_{\text{EW}} = 60 \text{ s}$			$\tau_{\text{EW}} = 120 \text{ s}$		
$\Omega_{90} \text{ (deg}^2\text{)}$	$\leq 100$	$\leq 10$	$\leq 1$	$\leq 100$	$\leq 10$	$\leq 1$	
HLA	0	0	0	0	0	0	
HLET	$9.3^{+20.1}_{-8.1} \times 10^1$	$3.0^{+10.0}_{-3.0} \times 10^0$	0	$4.3^{+10.3}_{-3.8} \times 10^1$	$1.0^{+4.0}_{-1.0} \times 10^0$	0	
CE20LA	$1.0^{+1.0}_{-1.0} \times 10^0$	0	0	0	0	0	
CE40LA	$1.0^{+1.0}_{-1.0} \times 10^0$	0	0	0	0	0	
CE20LET	$6.0^{+12.8}_{-5.1} \times 10^2$	$2.2^{+6.5}_{-1.9} \times 10^1$	0	$2.4^{+5.0}_{-2.1} \times 10^2$	$7.0^{+21.0}_{-7.0} \times 10^0$	0	
CE40LET	$9.4^{+19.9}_{-7.9} \times 10^2$	$6.1^{+12.0}_{-5.7} \times 10^1$	$1.0^{+2.0}_{-1.0} \times 10^0$	$5.1^{+10.8}_{-4.3} \times 10^2$	$1.9^{+4.7}_{-1.6} \times 10^1$	$0.0^{+1.0}_{-0.0} \times 10^0$	
CE4020A	$1.4^{+2.6}_{-1.3} \times 10^2$	$5.0^{+17.0}_{-5.0} \times 10^0$	$0.0^{+1.0}_{-0.0} \times 10^0$	$3.5^{+7.4}_{-3.2} \times 10^1$	$2.0^{+3.0}_{-2.0} \times 10^0$	0	
CE4020ET	$1.3^{+2.8}_{-1.1} \times 10^3$	$9.2^{+18.8}_{-8.3} \times 10^1$	$1.0^{+5.0}_{-1.0} \times 10^0$	$7.0^{+15.0}_{-5.9} \times 10^2$	$3.3^{+7.2}_{-2.9} \times 10^1$	$0.0^{+1.0}_{-0.0} \times 10^0$	
EW Time		$\tau_{\text{EW}} = 300 \text{ s}$			$\tau_{\text{EW}} = 600 \text{ s}$		
$\Omega_{90} \text{ (deg}^2\text{)}$	$\leq 100$	$\leq 10$	$\leq 1$	$\leq 100$	$\leq 10$	$\leq 1$	
HLA	0	0	0	0	0	0	
HLET	$1.0^{+29.0}_{-0.9} \times 10^1$	$0.0^{+1.0}_{-0.0} \times 10^0$	0	$0.0^{+5.0}_{-0.0} \times 10^0$	0	0	
CE20LA	0	0	0	0	0	0	
CE40LA	0	0	0	0	0	0	
CE20LET	$4.1^{+10.4}_{-3.7} \times 10^1$	$0.0^{+5.0}_{-0.0} \times 10^0$	0	$2.0^{+19.0}_{-2.0} \times 10^0$	0	0	
CE40LET	$8.3^{+18.9}_{-7.2} \times 10^1$	$1.0^{+10.0}_{-1.0} \times 10^0$	0	$7.0^{+31.0}_{-6.0} \times 10^0$	0	0	
CE4020A	$3.0^{+11.0}_{-3.0} \times 10^0$	0	0	0	0	0	
CE4020ET	$1.1^{+25.6}_{-1.0} \times 10^2$	$1.0^{+14.0}_{-1.0} \times 10^0$	0	$1.1^{+4.2}_{-0.9} \times 10^1$	0	0	

Table XVIII. # of NSBH mergers every year corresponding to Table 2 (Science Goal Requirements) of the CE White Paper. These numbers were calculated using the median local merger rates for NSBH (45 Gpc<sup>3</sup>yr<sup>-1</sup>).

Criteria	<b>0 XG</b>	<b>1 XG</b>			<b>2 XG</b>			<b>3 XG</b>
	HLA	HLET	CE40LA	CE20LA	CE4020A	CE40LET	CE20LET	CE4020ET
# at $z \leq 0.06$ with $\Delta\Omega \leq 0.1 \text{ deg}^2$	0	0	0	0	0	0	0	0
# at $0.06 < z \leq 0.1$ with $\Delta\Omega \leq 1 \text{ deg}^2$	2	3	3	3	5	6	5	6
# at $0.1 < z \leq 2$ with $\Delta\Omega \leq 10 \text{ deg}^2$	261	930	763	671	3260	7750	4942	16734
# at $z > 2$ with $\Delta\Omega \leq 100 \text{ deg}^2$	0	460	701	450	8163	24050	14826	39278
# at $z \geq 5$	0	95	1264	36	1880	2096	355	2748

## V. OPEN SCIENCE QUESTIONS UNIQUELY ADDRESS BY GRAVITATIONAL-WAVE OBSERVATIONS

A number of White Papers and design study reports have documented the science potential of current and future gravitational-wave observatories. For recent reviews see the following references []. In this Section we will summarize the science questions of interest to a diverse community of physicists and astronomers and could be addressed by gravitational-wave observations. In later sections, we will match these questions to specific networks that can answer them effectively.

- A. **Black holes and neutron stars throughout the cosmos**
- B. **Multimessenger astrophysics and dynamics of dense matter**

Neutron stars (NSs) are among the most exotic objects in the stellar graveyard. They are characterized by a unique relationship between the associated pressure and the energy density, called the equation of state (EoS). With the EoS, one can link the mass with the radius of the NS by solving the Tolman-Oppenheimer-Volkoff equation. NSs in binary configurations with a companion NS or BH can get tidally disrupted by the gravity of their companion close to the merger. The effect of the disruption on the phase of the GW waveform near merger can be described, to leading order, using the tidal deformability ( $\Lambda$ ) of the NS.  $\Lambda$  can be uniquely determined with the knowledge of the EOS and the mass of the NS. Inversely, the measurement of  $\Lambda$  and the mass of the NS from GW observations can be used to obtain constraints on the EOS that governs NS [citations needed].

The disruption of merging NSs in binaries can result in the production of non-relativistic to mildly-relativistic neutron-rich debris, and relativistic jets. This ejecta can power a variety of EM counterparts, including UV-optical-IR kilonovae [24–28], late-time radio flares from fast kilonova tails, gamma-ray bursts (GRBs), and their radio-to-X-ray afterglows AC: references need to be fixed. In this Section, we discuss the impact that XG detectors can have on our understanding of the dynamics of dense matter in NSs, and on the astrophysics of their ejecta and multi-messenger counterparts.

### 1. Multimessenger observations and early warnings

GW170817 is a spectacular example of a BNS merger for which GWs have been detected in association with an EM counterpart spanning all bands of the spectrum [29–32]. AC: references need to be fixed. These multi-messenger observations have painted a very detailed picture of the GW170817 progenitor and ejecta, and repre-

sent a golden example of the impact that GW discoveries can have on the field of time-domain astronomy.

GW observations of GW170817 have provided us information on its progenitor (including its total mass) AC: references need to be fixed. *Fermi* and *Integral* observations of GW170817 in gamma-rays have confirmed that at least some short GRBs are associated with BNS mergers. These observations also enabled measurement of the time delay between the merger (as determined by the GW signal) and the onset of the GRB emission (as determined by the gamma-ray light curve). Several physical mechanisms can contribute to this delay, including the engine delay (the time between the merger time and the time at which the jet from the central engine can be produced); the wind delay (the time required for the ejection of non-relativistic winds); the breakout delay (the time needed for jet to break out of the wind); the photospheric delay (the time needed for the jet to reach transparency). AC: cite here Lazzati’s recent frontiers review Future observations with XG GW detectors that can systematically unveil large samples of BNS mergers up to the peak of star formation could allow us to map progenitor properties to the physical conditions that enable the launch of successful relativistic jets (GRBs), and the physics that dominates the GW to gamma-ray time delay. This systematic mapping of GRBs to their progenitors is inaccessible to 4-km-long GW detectors due to the intrinsic limitation in their redshift reach AC: cite relevant results in Figures and Tables.

UV-optical-IR observations of the kilonova associated with GW170817 have enabled its arc-second localization, the identification of its host galaxy and redshift [29, 30], and confirmed that BNS mergers contribute to the production of heavy elements via r-process nucleosynthesis. Subsequent extensive follow-up observations of GW170817 from radio-to-X-rays have revealed the first off-axis GRB jet which, in turn, allowed us to probe its structure (energy-speed distribution of jet material as a function of polar angle from the jet) in an unprecedented way. This demonstrated that GRB jets are more complex than what typically assumed in modeling observations of cosmological events (these are preferentially observed on-axis due to observational selection effects). Specifically, GW170817 observations have shown that relativistic jets launched in BNS mergers can have “wings” (also referred to as “cocoon”) that enable the detection of EM emission even at relatively large viewing angles from the jet AC: references need to be fixed. AC: cite relevant results in Figures and Tables.

While 4 km-long GW detectors can build a sample of GW-kilonova associations in the local universe taking advantage of wide field-of-view optical telescopes such as Rubin and the Zwicky transient Facility, on theoretical grounds we expect that a zoo of EM counterparts should exist, ranging from optically bright and blue kilonovae associated perhaps with choked jets, to red and dim kilonovae associated with successful jet afterglows that, when viewed off-axis, can be more easily unveiled

at radio wavelengths. Hence, collecting a sample of at least a few BNS per year localized via GW observations to sky areas well matched to those of the smaller field of views of the most sensitive radio telescopes **AC: cite the relevant table** will offer a unique opportunity to probe the ejecta properties of BNSs in an optically un-biased way, and to characterize their diversity in relation to the properties of their progenitors. The exquisite localization capabilities of XG detectors (enabled by the same sensitivity that allows these detectors to reach the star formation peak) is needed to this end. **AC: references need to be fixed.**

The ability of XG detectors to localize BNS events to relatively small sky areas even before the merger occurs can also enable new discoveries. In fact, several GRBs are preceded by so-called gamma-ray precursors whose origin remains unclear. Moreover, several theoretical models predict prompt radio emission associated with compact object mergers, potentially generated by the NS magnetic field interactions during the in-spiral, by the interaction between a relativistic jet and the interstellar medium, or by the collapse of a supra-massive NS remnant into a BH. **AC: references need to be fixed.** All these scenarios strongly motivate precise sky localization and early-warning alerts to telescope before the merger [33]. With XG detectors, we can localize XX events per year within a sky area of XX. **AC: cite relevant table.**

## 2. Measuring the radius of the neutron star

Constraining NS radii is of significant importance because it provides crucial insights into the properties of the NS and the nature of matter inside it. Universal relations are empirical relationships between various physical properties of NSs, which are very instrumental in obtaining the NS radii from gravitational wave data. Gravitational waves contain information on tidal parameters like  $\tilde{\Lambda}$ , which can be used along with a few universal relations to constrain the radius. We describe the procedure for this below.

We use the GWBENCH [34] formalism to generate multi-dimensional Gaussian covariance matrices on the BNS population mentioned in Sec. III B. The universal relations described in [35–37] are then used to calculate individual tidal deformabilities  $\Lambda_1$  and  $\Lambda_2$  from the covariances obtained on the combined tidal deformability  $\tilde{\Lambda}$  and the mass ratio  $q$ . Another universal relation defined in [cite] is then used to infer the NS radii from the component tidal deformabilities.

We combine the events for every detector combination analysed in small mass bins to produce the effective radius error. For this, we make 20 mass bins from  $1 M_\odot$  to the maximum mass allowed by the EOS used in our study. We use the  $\sqrt{N}$  relationship for combining errors in radii in each mass bin separately [38].

## C. New sources, new probes and extreme astrophysics

Neutron stars and black holes can emit gravitational waves through a wide variety of mechanisms other than binary mergers and post-mergers [39, 40]. Although not yet detected, these other signals (with durations from a fraction of a second to longer than a human lifetime) have great discovery potential. When detected, especially in combination with signals carried by other messengers, these gravitational wave signals will reveal different populations of compact objects and probe extreme astrophysics in a regime largely different from that probed by compact binary mergers. Here we summarize scenarios for detection of and extraction of information from several predicted types of signals. We also note that the history of opening new windows of astronomy indicates that unexpected signals are to be expected.

### 1. Continuous waves

Spinning neutron stars produce *continuous gravitational waves*, signals with low amplitude compared to binary mergers but lasting many years [41, 42]. This allows for greatly enhanced detectability with matched filtering and similar techniques. Continuous gravitational wave emission likely is dominated by either a mass quadrupole (sustained by elastic or magnetic stresses) or a mass current quadrupole (produced by an unstable or weakly stabilized  $r$ -mode, a rotational mode with a frequency comparable to the star’s spin frequency). Free precession can also produce a changing mass quadrupole, but based on electromagnetic pulsar observations it is likely to be rare. For a given quadrupole, gravitational wave emission is stronger for rapidly rotating neutron stars, and the  $r$ -mode instability to gravitational wave emission is more likely to overcome various dissipation mechanisms at higher frequencies. Continuous gravitational wave searches are more sensitive when using the sky location, spin frequency, and other timing information of the source (if known). Sensitivities can be expressed in terms of a *sensitivity depth* [42, 43], which factors out the noise amplitude from everything else (methods, amount of data, etc.) and is convenient for extrapolating current searches to new detectors as we do here.

Accreting neutron stars are of particular interest as continuous wave sources since accretion tends to spin them up and to generate asymmetries through electron capture layers and lateral temperature gradients [44, 45], magnetic bottling of accreted material [46], or the gravitational wave-driven  $r$ -mode instability [47]. In fact one popular theory posits that the spins of accreting neutron stars are limited to relatively low values (compared to the maximum allowed for most equations of state) by the spin-down torque due to gravitational wave emission balancing the spin-up torque due to accretion [48]. In this case the gravitational wave strain of an accret-

ing neutron star is proportional to the square root of the observed x-ray flux [49], meaning that the brightest gravitational wave emitters are Sco X-1 and other low mass x-ray binaries with no observed pulsations and thus no confirmed spin frequency [50]. These sources exhibit stochastic x-ray variability, meaning that the accretion torque and spin frequency also fluctuate. Despite these obstacles, a recent gravitational wave search [51] achieved a sensitivity comparable to the strain implied by torque balance, even under pessimistic assumptions, albeit only in a narrow frequency band. Using the sensitivity depth of this search (a conservative  $39 \text{ Hz}^{-1/2}$ ) with the network noise curves from Table ?? and fluxes from a recent catalog [50], we find that the HLA network can detect gravitational waves at the torque balance limit of Sco X-1 at gravitational wave frequencies up to about 800 Hz. This corresponds to spin frequencies up to about 400 Hz for mass quadrupole emission or about 550 Hz for  $r$ -modes. Since accreting neutron stars are known to spin above 700 Hz in some cases, HLA is not guaranteed detection even of Sco X-1. With the 40LA configuration network, Cosmic Explorer is sensitive enough to detect at the torque balance limit up to 1400 Hz, high enough to cover almost all known neutron stars. The 4020ET configuration is sensitive up to almost 2 kHz, well beyond the gravitational wave frequency of any known neutron star. 4020ET is also sensitive to GX 5–1 and several other neutron stars up to almost 1 kHz. At this point even non-detection is very interesting since it strongly confronts the torque balance theory.

After accretion ends, the neutron star is believed to become a *millisecond pulsar* with high spin frequency and slow spin-down [52]. The latter indicates a small external magnetic dipole and small internal mass quadrupole by ruling out large torques due to electromagnetic radiation and gravitational waves respectively, and is usually believed to be dominated by magnetic dipole radiation. However in recent years it has become apparent that millisecond pulsar spin-downs exhibit a cutoff whose frequency dependence is quadrupolar rather than dipolar [53]. The implied minimum quadrupole is about  $10^{-9}$  times the moment of inertia, consistent with buried magnetic fields of order  $10^{11} \text{ G}$ , consistent with the fields of young pulsars and with theoretical predictions [46]. The buried magnetic field may survive for a long time under the accreted material [? ]. Millisecond pulsars which are observed regularly in radio or electromagnetic waves can be timed precisely enough to allow narrow, deep gravitational wave searches. Based on previous examples, the sensitivity depth of such a search can be conservatively estimated as  $500 \text{ Hz}^{-1/2}$  for a year of observation [42] and scales as the square root of the observation time. Then assuming an ellipticity of  $10^{-9}$  [53] and taking data from the ATNF pulsar catalog [54], the intrinsic strain is simple to determine [? ] and we can compare it to the search sensitivity with various networks. We find that with the HLA network one millisecond pulsar is detectable, while with the 4020ET network 21 are detectable. With the

HLA network one must have 12.5 years of data to detect 25 millisecond pulsars with ellipticity  $10^{-9}$ , and with the 4020A network only 1.75 years are needed to detect them. These numbers only include known pulsars; but by the time Cosmic Explorer is operational the Square Kilometre Array, Next Generation Very Large Array, and other instruments are expected to detect several gwbench pulsars for each one currently known [55? ]; so detectable numbers should improve accordingly. Conversely, non-detection would severely constrain the theory that millisecond pulsars’ original magnetic fields survive buried under accreted material.

It is also possible to perform all sky broadband continuous gravitational wave surveys for yet unknown neutron stars. In this case, recent population simulations [? ] for the Einstein Telescope indicate that it might detect more than 100 sources on its own. With its lower noise amplitude, a 40 km Cosmic Explorer will detect even more than Einstein Telescope. Any new continuous gravitational wave source detected by such surveys will be followed up with a year or more of observation, resulting in arcsecond sky localization (the diffraction limit for two astronomical units’ aperture) even with one interferometer, and a frequency measurement to tens of nHz. With such precise guidance the source is likely to be detected by electromagnetic pulsar searches.

The combination of continuous gravitational waves and electromagnetic observations will open new windows into neutron star interiors, and for a population distinct from the progenitors of binary mergers [56]. The ratio of gravitational wave frequency to spin frequency immediately yields insight into the gravitational wave emission mechanism (mass quadrupole, free precession, or  $r$ -mode). In the case of a mass quadrupole it might reveal the timescale of any coupling between crust and core leading to glitches (see below); and in the case of  $r$ -modes it can yield a measure of the neutron star’s compactness to a few percent [? ] and thus on the equation of state in a low temperature regime inaccessible to colliders. In some cases gravitational wave parallax can yield a distance measurement [57], and in others the distance can be obtained from electromagnetic astronomy. With the distance the magnitude of the quadrupole can be measured, and long term timing may indicate whether a mass quadrupole is sustained by elastic or magnetic forces. A large elastic quadrupole is only possible if the “neutron” star has an exotic composition [58], a magnetic quadrupole measurement yields an approximation of the star’s internal magnetic field, and an  $r$ -mode saturation amplitude is tied to viscosity and other microphysics of the stellar interior [59].

## 2. Core collapse supernovae

Core-collapse supernovae generate short bursts of gravitational waves from rapid motions of high density matter in their central regions. Unlike binary mergers, these mo-

tions cannot be predicted with sufficient precision for the use of matched filtering to detect the signals; but other techniques exist for detecting less modeled bursts. Simulations indicate that the most common events (little rotation, ???) will be detectable only in the Milky Way even with Cosmic Explorer, with uncommon events detectable in the Magellanic Clouds and very rare events perhaps detectable further away. Therefore the overall detection rate is expected to be of order one over the planned fifty year lifetime of the Cosmic Explorer facilities. Even one detected supernova will be a tremendous opportunity for multi-messenger astronomy, as was already seen with SN 1987A before gravitational wave astronomy existed.

### 3. Starquakes

#### D. Fundamental physics and precision measurement of the Hubble constant

The improved sensitivity of the Cosmic Explorer detectors in comparison to the current generation of GW detector networks results not only in more detections up to larger distances but also in a large number of signals with high SNRs, which are of immense importance for testing fundamental physics, general relativity and precise measurements of cosmological parameters.

##### 1. Testing general relativity and fundamental physics

The most general approach to testing general relativity involves the introduction of deviation parameters in the amplitude and phase of the GW waveform and constraining these parameters using observations [60][citations needed]. These deviation parameters are usually theory-agnostic but they can be mapped to specific theories if needed [61]. To a good approximation, constraints on these deviation parameters scale inversely with SNR  $\rho$ . When multiple GW observations are combined, the constraints on the deviation parameters also improve,

$$\sigma \propto \frac{1}{\rho} \longrightarrow \sum_{i=1}^N \frac{1}{\sigma^2} \propto \sum_{i=1}^N \rho^2 \quad (4)$$

where  $N$  is the number of GW events and  $\sigma$  is the standard deviation for a fiducial deviation parameter. The bounds on the deviation parameter will be affected by both, the number of signals detected by the network as well as the SNR with which these signals are detected. In Tab. I, we report the effective SNR ( $\sum \rho^2$ ) corresponding to BBH systems for different detector networks. Just going from an  $A^\sharp$  network to one containing a Cosmic Explorer detector improves the effective SNR by  $\sim 4 - 7$  times, improving the constraints by  $\sim 2 - 3$  times. Having at least two XG detectors in the network increases the effective SNR by two orders of magnitude compared to the  $A^\sharp$  network, leading to  $\sim 10$  times improvement

in the bounds on deviation parameters. We also report the number of BBH events with *post-inspiral* SNR greater than 100 and the effective post-inspiral SNR for each network. The post-inspiral SNR is calculated by performing the SNR calculation beginning at the ISCO (innermost stable circular orbit) frequency, instead of starting at  $f_{\text{low}}$ . Thus, it has contributions from the merger and the ringdown phases. While the network with three  $A^\sharp$  detectors is only expected to detect  $\mathcal{O}(10)$  events with post-inspiral SNR greater than 100, a network with CE20 will detect  $\mathcal{O}(100)$  and CE40 will detect  $\mathcal{O}(1000)$  such events every year. These events will allow testing general relativity in the strong-field regime close to merger and the use of quasinormal modes from the ringdown phase to test the nature of black holes.

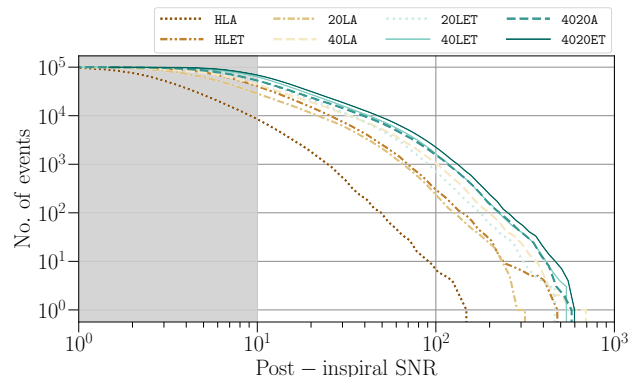


Figure 11. The PDF and scaled CDF plots for local BBH events.

These estimates can be extended to specific alternate theories of gravity (see Ref. [62] for a comprehensive study). Constraints on both the dipole radiation as well as the time variation of the gravitational constant  $G$  scale inversely with SNR. However, we should note that both these effects are low post-Newtonian (PN) order terms ( $-1\text{PN}$  and  $-4\text{PN}$ , respectively) and better localized using multiband observations with LISA, instead of only using ground-based networks. On the other hand, Lorentz violation with non-commutative theories of gravity and parity violation with the dynamical Chern-Simon theory affect the GW phasing at  $2\text{PN}$ , but the constraints on these theories scale with  $\rho^{-1/4}$ . On the other hand, theories that predict a massive graviton have a leading order effect on GW phase at  $1\text{PN}$ . While the constraint on the mass of the graviton scale as  $\rho^{-1/2}$  with SNR, they also scale as  $D_0^{-1/2}$ , where  $D_0$  is the cosmological distance. Thus, GWs from objects that are farther away can provide tighter bounds on the mass of graviton. In Tab. I, we list the number of BNS and BBH mergers that occur beyond  $z \geq 5$  and can be detected. For the BNS case, we see that only those networks that contain a 40 km Cosmic Explorer can detect such far-away mergers. The number of detections increase by 7 times when the network includes both CE40 and CE20 along with an  $A^\sharp$  detector, compared to only containing the CE40 with two

A<sup>#</sup> detectors. For BBH systems, the number of detections corresponding to systems that lie beyond  $z = 5$  increases by two orders of magnitude when only one of the Cosmic Explorer detectors are included, compared to a network with only A<sup>#</sup> detectors. Further, Fig. ?? shows that these distant events can be detected with SNRs  $\sim 100$  with Cosmic Explorer detectors. Thus, GW networks with Cosmic Explorer detectors will allow testing general relativity and fundamental physics for both theory-agnostic and theory-specific tests to unprecedented precision.

## 2. Measuring the Hubble constant with golden dark sirens and bright sirens

Detecting GWs from compact binary mergers allows the estimation of the luminosity distance and the sky position associated with the source [cite]. As GW observations provide the distance to the source without the need for external distance calibrators, GW sources are often referred to as standard candles. Under the construct of  $\Lambda$ CDM cosmology,

$$\begin{aligned} D_L &= \frac{1+z}{H_0} \int_{1/(1+z)}^1 \frac{dx}{x^2 \sqrt{\Omega_\Lambda + \Omega_m x^{-3}}} \\ &= \frac{1+z}{H_0} \int_{1/(1+z)}^1 \frac{dx}{x^2 \sqrt{1 - \Omega_m(1 - x^{-3})}}, \end{aligned} \quad (5)$$

where  $\Omega_m$  is the matter density,  $\Omega_\Lambda$  is the dark energy density, and we have used  $\Omega_\Lambda = 1 - \Omega_m$ . Thus, having obtained the distance to the source, if the redshift associated with the source can also be estimated, then these two quantities together can allow us to measure cosmological parameters, like the Hubble constant ( $H_0$ ). The utility of GWs in measuring  $H_0$  also becomes important in light of the Hubble tension [63, 64], which is the  $4\sigma - 6\sigma$  discrepancy between the early and the late universe measurements of  $H_0$  [65, 66]. Using GWs to constrain  $H_0$  is independent of the previously mentioned approaches and can help resolve the Hubble tension by measuring  $H_0$  to better than 2% precision.

Various approaches have been proposed in order to measure the redshift, and as a result,  $H_0$ , using GW observation. The neutron star(s) in BNS and NSBH mergers can undergo tidal disruption before the merger and lead to the generation of electromagnetic (EM) counterparts like kilonovae and short-gamma ray bursts, among others. Detecting these EM counterparts allows us to pinpoint the location of the merger and uniquely identify the host galaxy. Photometric or spectroscopic measurements of the galaxy provide the redshift associated with the source. This is referred to as the bright siren method. The BNS merger GW170817 [29–32] was the first event that was used to measure  $H_0$  with the bright siren approach, giving  $H_0 = 70_{-8}^{+12}$  km s<sup>-1</sup> Mpc<sup>-1</sup> [67].

In the absence of EM counterparts, as will be the case for BBH and some NSBH mergers, the sky localization

of the source can be utilized to obtain redshift measurement. The first such approach was proposed in Ref. [68], also called the statistical dark siren approach. It involves combining the  $H_0$  estimates from all the galaxies that lie within the localization volume associated with an event, for all the eligible detections. In doing so, the true value of  $H_0$  can be isolated from the noise and inferred. Combining 8 well-localized dark siren events, Ref. [69] obtain  $H_0 = 79.8_{-12.8}^{+19.1}$  km s<sup>-1</sup> Mpc<sup>-1</sup>. These bounds are expected to get better with more detections. Figs. ?? and 8 show the accuracy in the measurement of the luminosity distance and the 90%–credible sky area for BBH and NSBH, respectively. In comparison to the HLA network, the inclusion of XG detectors in the network results in drastically better localization estimates. In particular, Tab. I lists the number of BBH detections that can be localized to  $\Delta D_L/D_L \leq 10\%$  and  $\Omega_{90} \leq 10\text{deg}^2$ . The number of such events increases by  $\sim 5$  times with 1 XG,  $\sim 50$  with 2 XG, and  $\sim 100$  times with 3 XG detectors.

Among these dark siren events, there will also be a few a fraction of events that are so well localized in the sky that only one galaxy can lie in that sky patch [70]. This would ensure unique identification of the host galaxy and the associated redshift can be obtained. Such events are called golden dark siren events. In Fig. 15, we show the accuracy with which  $H_0$  can be estimated using the golden dark siren approach and the bright siren approach for different detector networks. We follow Refs. [71, 72] to categorize those BBH and NSBH events as golden dark sirens for which  $z \leq 1$  and  $\Omega_{90} \leq 0.04 \text{deg}^2$ . To calculate the fractional errors in  $H_0$ , we convert the luminosity distance errors to  $H_0$  errors using equation 5. Following Ref. [72] we neglect the errors in the redshift measurement, but take into account the uncertainty in the value of  $\Omega_m$ . Specifically, Planck gives  $\Omega_m = 0.315 \pm 0.007$  [66] and the SH0ES measurement of  $q_0$  is used to give  $\Omega_m = 0.327 \pm 0.016$  [65]. This information is included in the Fisher analysis by applying a Gaussian prior on  $\Omega_m$  standard deviation given by

$$\sigma_{\Omega_m} = \sqrt{\sigma_{\text{Planck}}^2 + \sigma_{\text{SH0ES}}^2} = 0.017. \quad (6)$$

The Fisher matrix obtained by combining estimates from  $N$  golden dark siren events is given by

$$\Gamma_{ij} = \sum_{k=1}^N \frac{1}{\sigma_{D_L}^2} \left( \frac{\partial D_L}{\partial \theta_i} \right) \left( \frac{\partial D_L}{\partial \theta_j} \right) \Big|_k + \delta_{i2} \delta_{j2} \frac{1}{\sigma_{\Omega_m}^2}, \quad (7)$$

with  $\theta = (H_0, \Omega_m)$ . From Fig. 2, we see that the chosen redshift distribution allows for 10 BBH and 20 NSBH mergers within  $z = 0.1$  every year. To avoid making conclusions based on a specific set of events, we perform 100 realizations of the universe and calculate the combined estimates for each of these realizations. Fig. 15 shows the median error in  $H_0$  and the error bars portray the 68% confidence interval.

For the bright siren approach, we consider those BNS for which  $z \leq 0.3$  and  $\Omega_{90} \leq 10 \text{deg}^2$ . The redshift range

takes into account the redshift up to which a kilonova can be observed using the Rubin or the Roman telescope [citation needed] and the cut on sky-area matches the field of view of the Rubin observatory. We also assume a 20% duty-cycle due to the time-sensitive follow-up required for this method. Following the same steps as for the golden dark siren case, we estimate the fractional errors in  $H_0$  using the bright siren approach, which are also shown in Fig. 15. For both the bright siren and the golden dark siren cases, we multiply the errors by a factor of  $\sqrt{2}$ , in order to account for systematic effects that have not been included in this work.

[Write about the inference from the plots.]

### 3. Measuring the $\Lambda$ CDM with NS tides

BNS have an intrinsic mass scale and can only exist in a narrow range of masses. This mass scale is imprinted in the tidal interaction between the component NSs. Therefore, if the nuclear EoS is known, one can determine the source-frame masses by a measurement of the tidal deformability. This, in turn, would allow the measurement of the redshift directly from a GW observation because it is the redshifted mass that is inferred from the point-particle approximation of the waveform. Such a method was first proposed in [73] and further explored in [74, 75]. A measurement of the Hubble constant using a known relationship between the tidal parameter and source-frame mass was explored in [76–78] while [79] showed that one can simultaneously estimate both the nuclear EoS and the Hubble constant using future observatories. A measurement of the dark energy EoS was explored in [80, 81].

In this section, we explore the potential of different XG configurations to constrain the expansion history of the Universe assuming that the nuclear EoS is known. It is found in [77] that up to a 15% uncertainty in the knowledge of the EoS does not affect the measurement of the Hubble constant in a meaningful manner. We use the TaylorF2 waveform model augmented with the 5PN and 6PN tidal terms in the phase, terminating the signal at the ISCO frequency corresponding to the total mass of the binary. Additionally, we assume the APR4 EoS for the NS. We fit the logarithm (base 10) of the tidal deformability as a function of the mass of the NS using a fifth-order polynomial given by

$$\log_{10} \Lambda(m) =, \quad (8)$$

where  $m$  is in units of  $M_\odot$ . We verify that the fit reproduces the slope of the curve accurately with maximum errors at a few percent around the double Gaussian from which the neutron star masses are drawn. This is crucial because it is the slope of the curve that contributes to the Fisher errors on the redshift.

The Fisher errors from the  $d_L$ - $z$  space are then propagated to the space of cosmological parameters,  $\vec{\phi}$ , via

another Fisher matrix given by [82]

$$\mathcal{G}_{ij} = \sum_{k=1}^N \frac{1}{\sigma_{d_L,k}^2} \frac{\partial d_L^k(z)}{\partial \phi^i} \frac{\partial d_L^k(z)}{\partial \phi^j}, \quad (9)$$

where  $N$  is the total number of observations in the catalog and  $\sigma_{d_L,k}^2$  is the total variance in the luminosity distance for the  $k$ -th event given by

$$(\sigma_{d_L})^2 = (\sigma_{d_L}^h)^2 + (\sigma_{d_L}^z)^2. \quad (10)$$

Here,  $\sigma_{d_L}^h$  is the contribution to the luminosity distance error due to the error in the GW amplitude while  $\sigma_{d_L}^z$  is that due to the error in the redshift measurement, given by

$$\sigma_{D_L}^z = \left| \frac{\partial D_L}{\partial z} \right| \sigma_z. \quad (11)$$

In writing Eq. 9, we have neglected the correlations in the  $d_L$ - $z$  space for simplicity.

The results for  $H_0$  and  $\Omega_M$  are shown in Fig. 12. It is observed that the Hubble constant and dark matter energy density cannot be simultaneously constrained in the absence of any XG detectors. With at least 1 XG detector,  $H_0$  can be determined at the percent level while  $\Omega_M$  can be measured to an accuracy of 5–10%. Of particular note is that a XG network consisting of a 20 km CE detector is significantly worse than its 40 km counterpart and an ET. With a network of 2 XG detectors, the errors decrease by a factor of 2–4 while a full XG network consisting of 3 CG detectors further reduces the errors by another 50%.

### 4. Measuring the dark energy with NS tides

The results for the dark energy equation of state parameters are shown in Fig. 13. In the absence of any XG detectors, dark energy equation of state parameters cannot be measured. We see similar factors of improvement with the addition of each XG detector. Notably, if the  $\Lambda$ CDM parameters are marginalised over instead of assumed to be given from other experiments, the constraints on the dark energy equation of state parameters worsen by a factor of 5–10.

### 5. Gravitational-wave lensing

Gravitational lensing, a captivating phenomenon predicted by Einstein’s theory of general relativity, bends light and gravitational radiation as they pass near massive intervening objects. The advent of third generation detectors ushers in a new era of gravitational lensing exploration, as it is projected that approximately one in a thousand binary black holes and one in a few thousand binary neutron stars will be strongly lensed, resulting in an

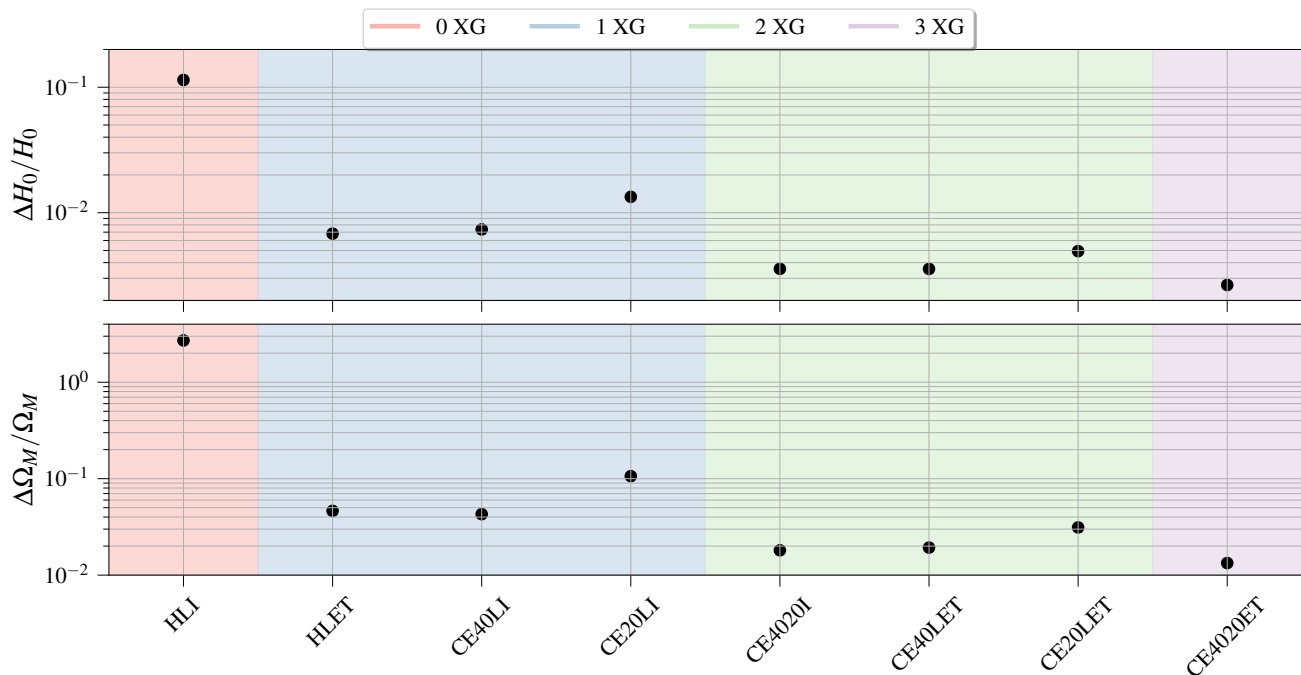


Figure 12. The fractional error in the Hubble constant  $H_0$  and the dark matter energy density parameter  $\Omega_M$  for the various network configurations under consideration.

Table XIX. Relative rate of strong lensing detections per year for seven detector networks and variable binary compact object population models. The strong lenses are generated using galaxies drawn from the SDSS galaxy catalog [see 83].

Detector configuration	Local population	Population III	Primordial black holes	Binary neutron stars
HLET	$6.9 \times 10^{-3}$	$2.3 \times 10^{-3}$	$2.0 \times 10^{-3}$	$2.7 \times 10^{-4}$
20LA	$6.6 \times 10^{-4}$	$2.2 \times 10^{-3}$	$2.1 \times 10^{-3}$	$1.5 \times 10^{-4}$
40LA	$7.3 \times 10^{-4}$	$2.4 \times 10^{-3}$	$2.1 \times 10^{-3}$	$2.4 \times 10^{-4}$
40LET	$7.9 \times 10^{-4}$	$2.5 \times 10^{-3}$	$2.2 \times 10^{-3}$	$2.4 \times 10^{-4}$
20LET	$7.3 \times 10^{-4}$	$2.3 \times 10^{-3}$	$2.2 \times 10^{-3}$	$2.5 \times 10^{-4}$
4020A	$7.6 \times 10^{-4}$	$2.5 \times 10^{-3}$	$2.2 \times 10^{-3}$	$2.4 \times 10^{-4}$
4020ET	$8.1 \times 10^{-4}$	$2.5 \times 10^{-3}$	$2.3 \times 10^{-3}$	$2.3 \times 10^{-4}$

annual detection rate of around  $\mathcal{O}(50-100)$  lensed events (see Table XIX). Such lensed detections have the potential to achieve highly precise localization of binary black holes with sub-arcsecond accuracy, identify new subpopulations of lensed systems, probe the fundamental properties of gravitational waves, reconstruct gravitational lenses using gravitational wave signals, perform cosmographic measurements at submillisecond timing precision, develop comprehensive models of lens populations, and conduct multifaceted studies involving multiple messenger signals [see 84, 85, and references therein]. Embracing this research frontier with third generation detectors not only advances gravitational wave astronomy but can also pave the way for groundbreaking discoveries that enhance our knowledge of gravity, astrophysics, and

the intricacies of the universe.

## E. Dark matter, early universe and physics beyond the standard model

### 1. Stochastic backgrounds

The sensitivity of a given XG network to the stochastic gravitational-wave background of primordial origin quantifies its ability to probe early-universe physics. Typical stochastic background searches assume that the background is Gaussian, isotropic, stationary, and unpolarized, so that the optimal search strategy is to look for ex-

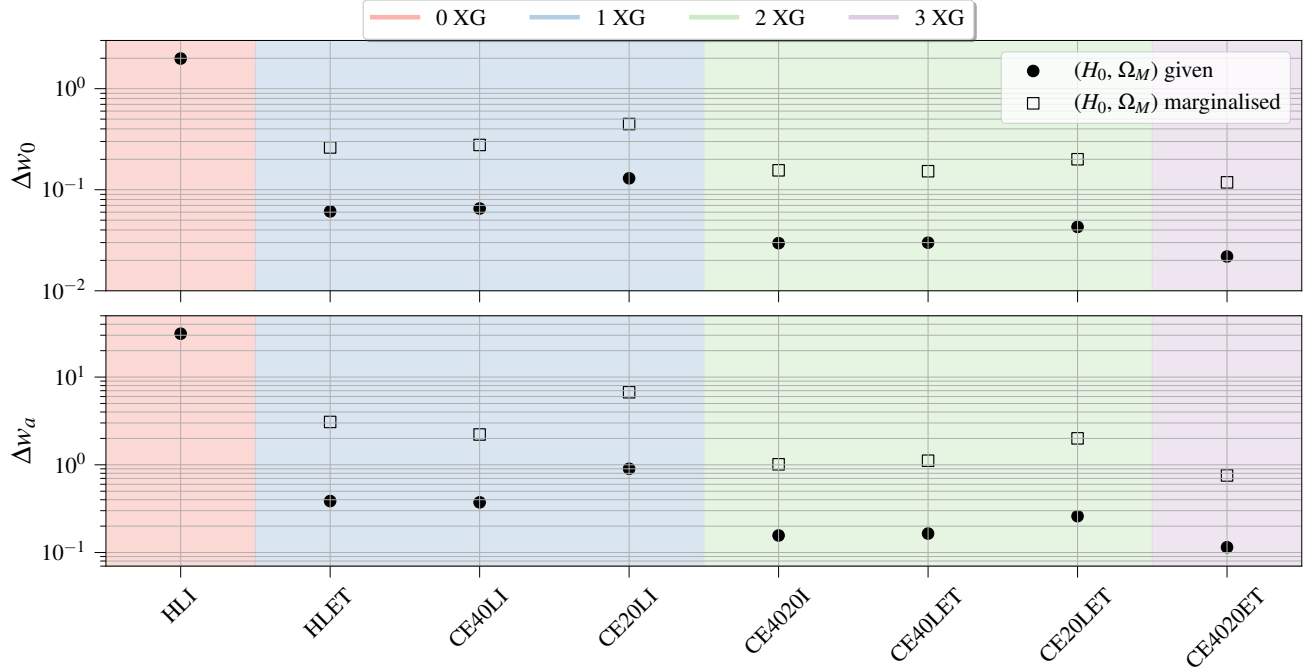


Figure 13. The error in the dark energy equation of state parameters  $w_0$  and  $w_\alpha$  for the various network configurations under consideration.

cess correlated power between pairs of detectors [86, 87]. In this case, the sensitivity of the pair depends primarily on the detector PSDs and geometry, quantified via the overlap reduction function,  $\gamma(f)$  [88]. Co-located and co-aligned detectors have  $\gamma(f) = 1$ , while for detectors separated by large distances and large relative angles,  $\gamma(f)$  is an oscillatory function that asymptotes to zero at large frequencies, penalizing the sensitivity of that detector baseline. The overlap reduction functions for several detector baselines considered in this document are shown in the right panel of Fig. 14.

The strength of the stochastic background is typically parameterized in terms of

$$\Omega_{\text{GW}}(f) \equiv \frac{1}{\rho_c} \frac{d\rho_{\text{GW}}}{d \ln f} = \Omega_\alpha \left( \frac{f}{f_{\text{ref}}} \right)^\alpha, \quad (12)$$

where  $\rho_{\text{GW}}$  is the energy density in gravitational waves and  $\rho_c$  is the critical energy density needed to close the universe. For a given value of the power-law index  $\alpha$ , the background amplitude that would be detectable with SNR  $\rho$  and an observing time  $T$  is given by

$$\Omega_\alpha = \frac{\rho}{\sqrt{2T}} \left[ \int_{f_{\text{min}}}^{f_{\text{max}}} df \frac{(f/f_{\text{ref}})^{2\alpha}}{\Omega_{\text{eff}}^2(f)} \right]^{-1/2} \quad (13)$$

$$\Omega_{\text{eff}} = \frac{10\pi^2}{3H_0^2} f^3 S_{\text{eff}}(f). \quad (14)$$

The effective strain noise power spectral density is given

by

$$S_{\text{eff}} = \left[ \sum_{I=1}^M \sum_{J>I}^M \frac{\gamma_{IJ}^2(f)}{P_{n,I}(f)P_{n,J}(f)} \right]^{-1/2} \quad (15)$$

where the indices  $I, J$  indicate the interferometer and  $P_n$  is the noise PSD.

The last row of Table I gives the background amplitude that would be detectable with SNR=3 after one year of observing for each of the eight networks considered in this document at a reference frequency of 25 Hz for  $\alpha = 0$ , which is the theoretical expectation for backgrounds produced by vanilla inflation [89]. The left panel of Fig. 14 shows the power-law integrated (PI) curves [90] for each network, for which a stochastic background that crosses or lies tangent to the PI curve would be detected with SNR=3 after 1 yr of observing.

Because ET consists of three nearly co-located detectors and has the best projected sensitivity at low frequencies, the networks including ET are not penalized as strongly by the geometric  $\gamma(f)$  factor and thus have the best projected sensitivity to the stochastic background. We neglect the effect of correlated noise, which may be significant for the co-located ET detectors [e.g., 91]. The exact sensitivity of the proposed XG networks will change due to the change in the overlap reduction function once the locations and orientations of the detectors are finalized, but the numbers quoted here are meant to be representative of XG detector capabilities.

It is worth noting that these values of  $\Omega_{\text{GW}}$  are calculated assuming that the primordial background can be

perfectly separated from the foreground of merging compact binaries. New methods that exploit the statistical differences between the two signals are being developed to ensure this is possible by the time that XG data becomes available [92–96].

### F. Axion clouds around rotating black holes

If ultralight bosonic dark matter exists, it could appear spontaneously near rotating black holes, be bound to them if the Compton wavelength is comparable to the black hole size, and extract mass and energy from them over time, building up a macroscopic dark-matter “cloud” via a superradiance process [97, 98]. The so-called “gravitational atom” could then emit quasi-monochromatic, persistent gravitational waves via boson-boson annihilation [99]. Sensitivity towards these boson cloud systems has reached the galactic center in the most recent ob-

serving only for quite young spinning black holes (less than  $10^5$  years) [100], but with the advent of XG detectors, those prospects will improve at least 10-20x. In Fig. ??, we plot the distance reach, computed according to an analytic expression, Eq. 57, given in [101], as a function of ultralight boson mass, in the small gravitational fine-structure constant  $\alpha$  limit ( $\alpha < 0.1$ ), assuming a uniform distribution of spins between  $[0.2, 0.9]$ , a LogUniform distribution of ages between  $[10^3, 10^7]$  years, a coherence length of 10 days, a Kroupa distribution for black hole masses between  $[5, 100]M_\odot$ . This distance corresponds to detecting at least 5% of black holes located at that distance away with a particular boson cloud. The improvements relative to the current detector era are immense, and are derived for a *semi-coherent* all-sky search for boson cloud systems with FFT length  $T_{\text{FFT}} = 10$  days and a threshold on our detection statistic, the critical ratio, of 3.4, as done in a similar analysis for Einstein Telescope design comparisons [102].

- 
- [1] Evan D. Hall and Matthew Evans. Metrics for next-generation gravitational-wave detectors. *Class. Quant. Grav.*, 36(22):225002, 2019.
- [2] Matthew Evans et al. A Horizon Study for Cosmic Explorer: Science, Observatories, and Community. 9 2021.
- [3] Post-O5 Study Group. Report from the lsc post-o5 study group. Technical Report T2200287, LIGO, 2022.
- [4] M. Punturo et al. The Einstein Telescope: A third-generation gravitational wave observatory. *Class. Quant. Grav.*, 27:194002, 2010.
- [5] R. Abbott et al. GWTC-3: Compact Binary Coalescences Observed by LIGO and Virgo During the Second Part of the Third Observing Run. 11 2021.
- [6] R. Abbott et al. Population of Merging Compact Binaries Inferred Using Gravitational Waves through GWTC-3. *Phys. Rev. X*, 13(1):011048, 2023.
- [7] Piero Madau and Mark Dickinson. Cosmic Star Formation History. *Ann. Rev. Astron. Astrophys.*, 52:415–486, 2014.
- [8] Cecilio García-Quirós, Marta Colleoni, Sascha Husa, Héctor Estellés, Geraint Pratten, Antoni Ramos-Buades, Maite Mateu-Lucena, and Rafel Jaume. Multimode frequency-domain model for the gravitational wave signal from nonprecessing black-hole binaries. *Phys. Rev. D*, 102(6):064002, 2020.
- [9] Ken K. Y. Ng, Salvatore Vitale, Will M. Farr, and Carl L. Rodriguez. Probing multiple populations of compact binaries with third-generation gravitational-wave detectors. *Astrophys. J. Lett.*, 913(1):L5, 2021.
- [10] Ken K. Y. Ng, Gabriele Franciolini, Emanuele Berti, Paolo Pani, Antonio Riotto, and Salvatore Vitale. Constraining High-redshift Stellar-mass Primordial Black Holes with Next-generation Ground-based Gravitational-wave Detectors. *Astrophys. J. Lett.*, 933(2):L41, 2022.
- [11] Will M. Farr and Katerina Chatziioannou. A Population-Informed Mass Estimate for Pulsar J0740+6620. *Research Notes of the American Astronomical Society*, 4(5):65, May 2020.
- [12] Rubin observatory system & lsst survey key numbers, Last accessed 3 October 2022.
- [13] Željko Ivezić et al. LSST: from Science Drivers to Reference Design and Anticipated Data Products. *Astrophys. J.*, 873(2):111, 2019.
- [14] R. Scaramella et al. Euclid preparation - I. The Euclid Wide Survey. *Astron. Astrophys.*, 662:A112, 2022.
- [15] A. Rau et al. The Hot and Energetic Universe: The Wide Field Imager (WFI) for Athena+. *arXiv e-prints*, page arXiv:1308.6785, August 2013.
- [16] R. Hounsell et al. Simulations of the WFIRST Supernova Survey and Forecasts of Cosmological Constraints. *Astrophys. J.*, 867(1):23, 2018.
- [17] Eve A. Chase, Brendan O’Connor, Christopher L. Fryer, Eleonora Troja, Oleg Korobkin, Ryan T. Wollaeger, Marko Ristic, Christopher J. Fontes, Aimee L. Hungerford, and Angela M. Herring. Kilonova Detectability with Wide-field Instruments. *Astrophys. J.*, 927(2):163, 2022.
- [18] E. J. Murphy, A. Bolatto, S. Chatterjee, C. M. Casey, L. Chomiuk, D. Dale, I. de Pater, M. Dickinson, J. D. Francesco, G. Hallinan, A. Isella, K. Kohno, S. R. Kulkarni, C. Lang, T. J. W. Lazio, A. K. Leroy, L. Loinard, T. J. Maccarone, B. C. Matthews, R. A. Osten, M. J. Reid, D. Riechers, N. Sakai, F. Walter, and D. Wilner. The ngVLA Science Case and Associated Science Requirements. In Eric Murphy, editor, *Science with a Next Generation Very Large Array*, volume 517 of *Astronomical Society of the Pacific Conference Series*, page 3, December 2018.
- [19] Chandra x-ray observatory: Mission characteristics, Last accessed 3 October 2022.
- [20] Jessica A. Gaskin et al. Lynx X-Ray Observatory: an overview. *Journal of Astronomical Telescopes, Instruments, and Systems*, 5:021001, April 2019.
- [21] David N. Burrows et al. Swift X-Ray Telescope. In Kathryn A. Flanagan and Oswald H. Siegmund, editors, *X-Ray and Gamma-Ray Instrumentation for Astronomy XI*, volume 4140 of *Society of Photo-Optical*

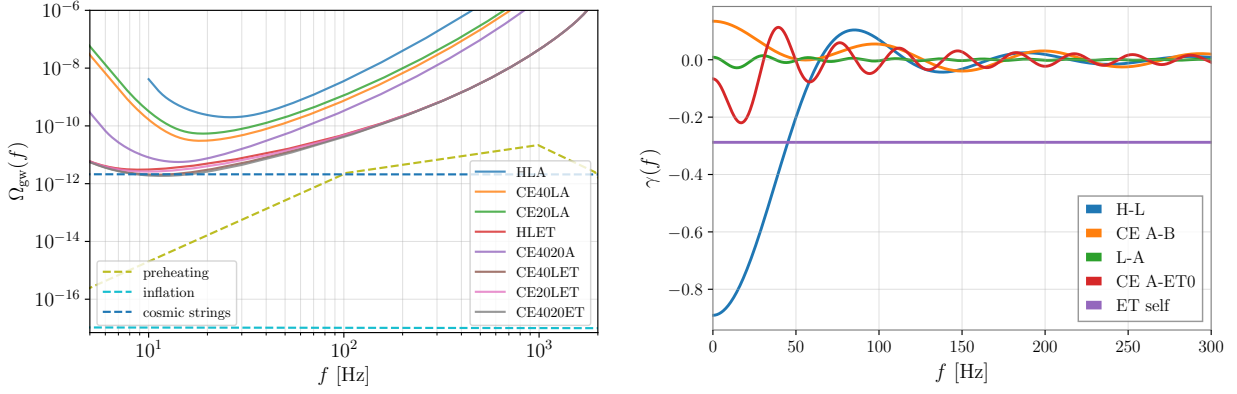


Figure 14. *Left*: Power-law integrated (PI) curves showing the sensitivity of the various detector networks considered in this work to the stochastic gravitational-wave background. Any background whose spectrum crosses the PI curve would be detected with  $\text{SNR}=3$  after one year of observing time. Dashed lines show the expected backgrounds for cosmic strings ( $G\mu = 10^{-11}$  with fiducial model parameters from Ref. [103]), preheating (for hybrid inflation occurring at  $10^9$  GeV as calculated in Ref. [104]), and standard slow-roll inflation. *Right*: Overlap reduction functions for various detector pairs considered here.

- Instrumentation Engineers (SPIE) Conference Series*, pages 64–75, December 2000.
- [22] K Bundy, K Westfall, N MacDonald, R Kupke, M Savage, C Poppett, A Alabi, G Becker, J Burchett, P Capak, et al. Fobos: A next-generation spectroscopic facility at the wm keck observatory. *arXiv preprint arXiv:1907.07195*, 2019.
- [23] R. A. Perley, C. J. Chandler, B. J. Butler, and J. M. Wrobel. The Expanded Very Large Array: A New Telescope for New Science. , 739(1):L1, September 2011.
- [24] Li-Xin Li and Bohdan Paczynski. Transient events from neutron star mergers. *Astrophys. J. Lett.*, 507:L59, 1998.
- [25] Brian D. Metzger. Kilonovae. *Living Rev. Rel.*, 23(1):1, 2020.
- [26] J. Goodman. Are gamma-ray bursts optically thick? *Astrophys. J. Lett.*, 308:L47–L50, 1986.
- [27] David Eichler, Mario Livio, Tsvi Piran, and David N. Schramm. Nucleosynthesis, Neutrino Bursts and Gamma-Rays from Coalescing Neutron Stars. *Nature*, 340:126–128, 1989.
- [28] Koutarou Kyutoku, Masaru Shibata, and Keisuke Taniguchi. Coalescence of black hole–neutron star binaries. *Living Rev. Rel.*, 24(1):5, 2021.
- [29] B. P. Abbott et al. GW170817: Observation of Gravitational Waves from a Binary Neutron Star Inspiral. *Phys. Rev. Lett.*, 119(16):161101, 2017.
- [30] B. P. Abbott et al. Multi-messenger Observations of a Binary Neutron Star Merger. *Astrophys. J. Lett.*, 848(2):L12, 2017.
- [31] B. P. Abbott et al. Gravitational Waves and Gamma-rays from a Binary Neutron Star Merger: GW170817 and GRB 170817A. *Astrophys. J. Lett.*, 848(2):L13, 2017.
- [32] B. P. Abbott et al. Estimating the Contribution of Dynamical Ejecta in the Kilonova Associated with GW170817. *Astrophys. J. Lett.*, 850(2):L39, 2017.
- [33] Surabhi Sachdev et al. An Early-warning System for Electromagnetic Follow-up of Gravitational-wave Events. *Astrophys. J. Lett.*, 905(2):L25, 2020.
- [34] Ssohrab Borhanian. GWBENCH: a novel Fisher information package for gravitational-wave benchmarking. *Class. Quant. Grav.*, 38(17):175014, 2021.
- [35] Katerina Chatziioannou, Carl-Johan Haster, and Aaron Zimmerman. Measuring the neutron star tidal deformability with equation-of-state-independent relations and gravitational waves. *Phys. Rev. D*, 97(10):104036, 2018.
- [36] Kent Yagi. Multipole love relations. *Phys. Rev. D*, 89:043011, Feb 2014.
- [37] Kent Yagi and Nicolás Yunes. Approximate Universal Relations for Neutron Stars and Quark Stars. *Phys. Rept.*, 681:1–72, 2017.
- [38] Rachael Huxford, Rahul Kashyap, Ssohrab Borhanian, Arnab Dhani, and B.S. Sathyaprakash. Dense matter equation of state with cosmic explorer and einstein telescope in preparation., 2023.
- [39] Kostas Glampedakis and Leonardo Gualtieri. Gravitational waves from single neutron stars: an advanced detector era survey. *Astrophys. Space Sci. Libr.*, 457:673–736, 2018.
- [40] Vassiliki Kalogera et al. The Yet-Unobserved Multi-Messenger Gravitational-Wave Universe. 3 2019.
- [41] Keith Riles. Searches for continuous-wave gravitational radiation. *Living Rev. Rel.*, 26(1):3, 2023.
- [42] Karl Wette. Searches for continuous gravitational waves from neutron stars: A twenty-year retrospective. 5 2023.
- [43] Christoph Dreissigacker, Reinhard Prix, and Karl Wette. Fast and Accurate Sensitivity Estimation for Continuous-Gravitational-Wave Searches. *Phys. Rev. D*, 98(8):084058, 2018.
- [44] Lars Bildsten. Gravitational radiation and rotation of accreting neutron stars. *Astrophys. J. Lett.*, 501:L89, 1998.
- [45] T. J. Hutchins and D. I. Jones. Gravitational radiation from thermal mountains on accreting neutron stars: sources of temperature non-axisymmetry. *Mon. Not. Roy. Astron. Soc.*, 522(1):226–251, 2023.
- [46] Andrew Melatos and D. J. B. Payne. Gravitational radiation from an accreting millisecond pulsar with a magnetically confined mountain. *Astrophys. J.*, 623:1044–

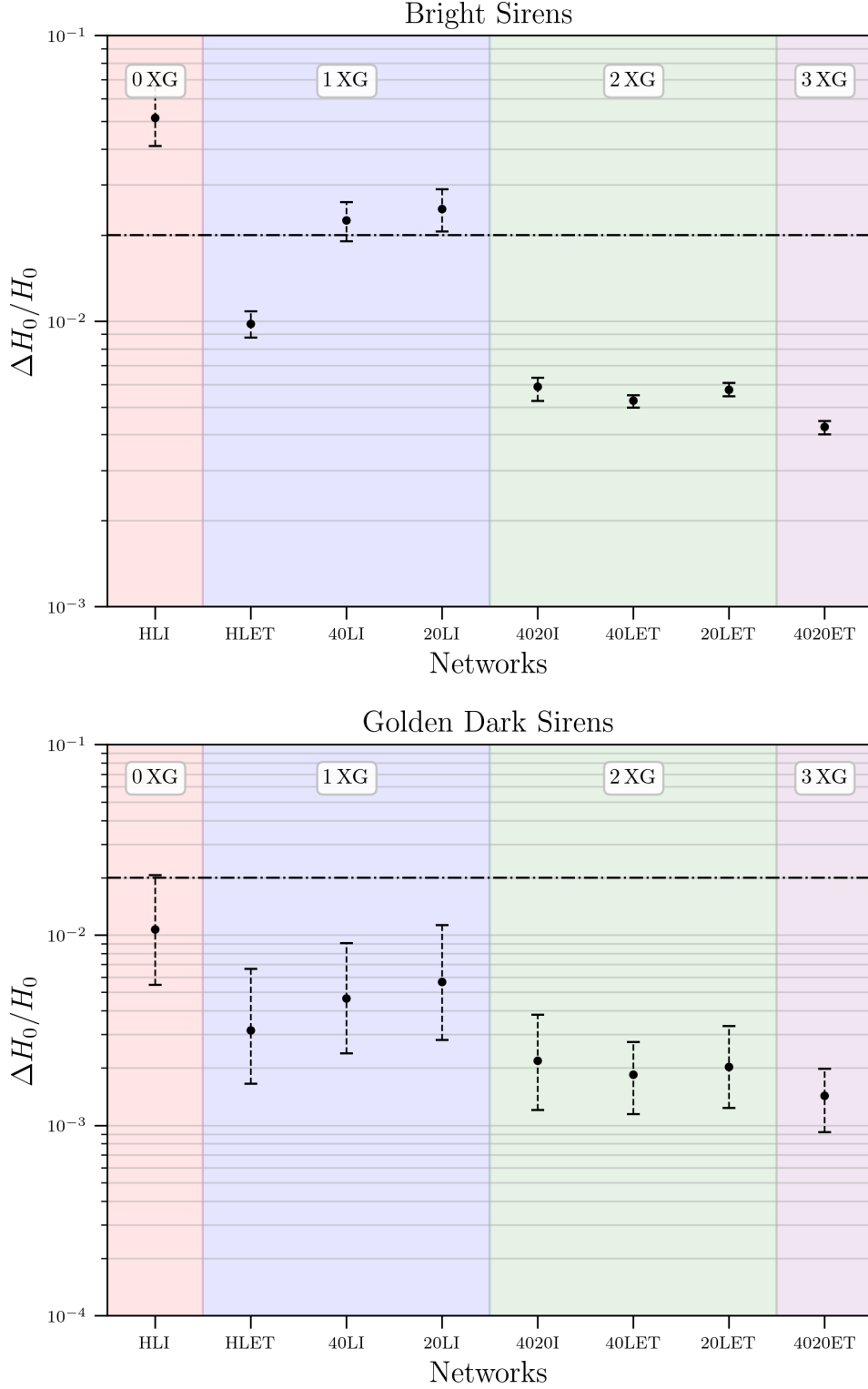


Figure 15. The accuracy in  $H_0$  measurement using the bright siren approach with BNS mergers and the golden dark siren approach with BBH mergers. For the golden dark siren approach, we consider BBH systems that lie within  $z = 0.1$  and are localized in the sky to  $\Omega_{90} \leq 0.04 \text{ deg}^2$ . Fig. ?? estimates 10 BBH mergers within a redshift of  $z = 0.1$  every year. Thus, we perform multiple realizations of our universe to obtain multiple sets of these 10 events and convert the distance errors from these events to errors in  $H_0$  (assuming a Gaussian prior on  $\Omega_m$  with width  $\sigma = 0.017$ , informed by the Planck and SH0ES estimates). The markers show the median  $H_0$  accuracy across multiple realizations and the errorbars show the 68% confidence interval. For the bright siren method, we restrict to BNS mergers within  $z = 0.3$  that are localized in the sky to  $\Omega_{90} \leq 10 \text{ deg}^2$ . We also include a duty cycle of 20% for the bright siren method, taking into account the time-sensitive follow-up that is needed for such events. The errors of both the golden dark siren and the bright siren approaches are worsened by a factor of  $\sqrt{2}$ , to account for systematics that might be missed in these calculations.

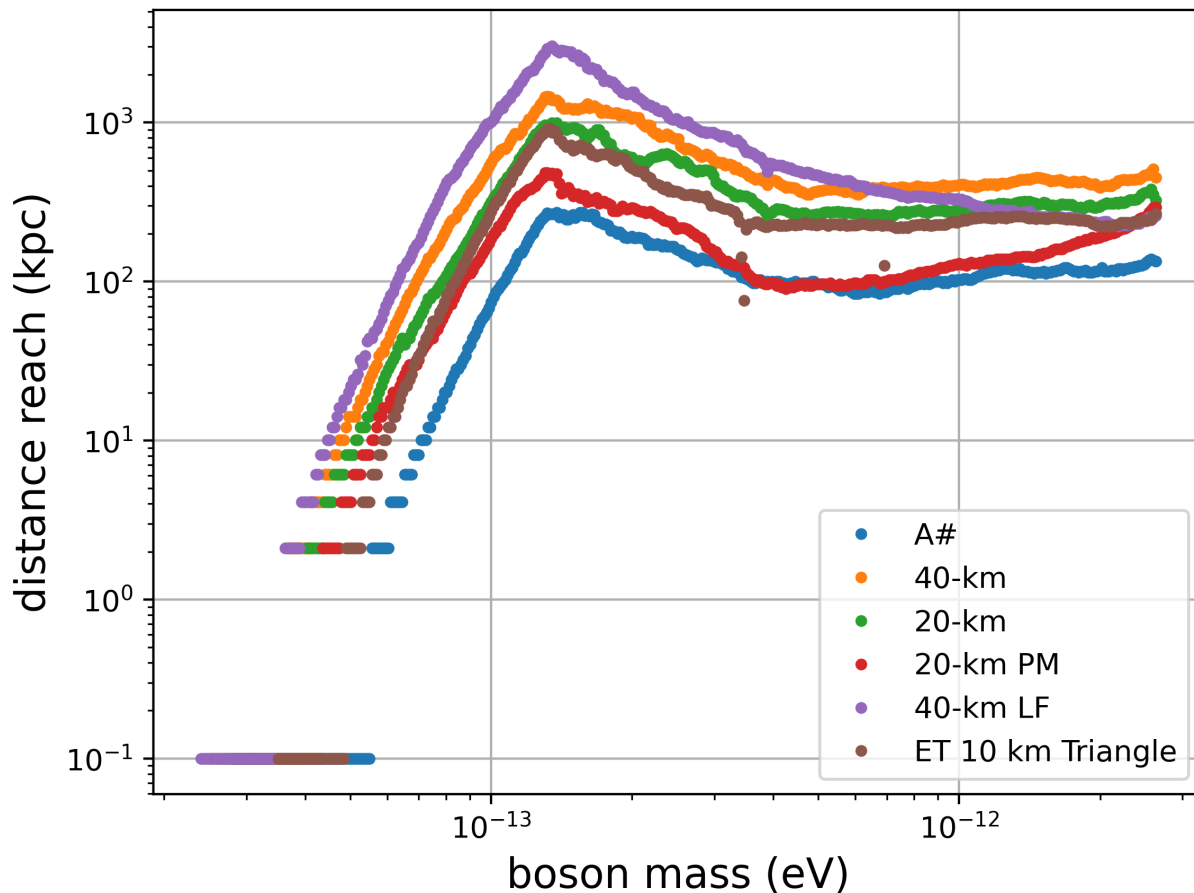


Figure 16. Astrophysical distance reach as a function of axion mass for ultralight boson clouds that could form around rotating black holes. Different colors correspond to different detectors.

- 1050, 2005.
- [47] Nils Andersson, Kostas D. Kokkotas, and Nikolaos Stergioulas. On the relevance of the  $r$  mode instability for accreting neutron stars and white dwarfs. *Astrophys. J.*, 516:307, 1999.
- [48] J. Papaloizou and J. E. Pringle. Gravitational radiation and the stability of rotating stars. *Mon. Not. Roy. Astron. Soc.*, 184:501–508, August 1978.
- [49] R. V. Wagoner. GRAVITATIONAL RADIATION FROM ACCRETING NEUTRON STARS. *Astrophys. J.*, 278:345–348, 1984.
- [50] A. Avakyan, M. Neumann, A. Zainab, V. Doroshenko, J. Wilms, and A. Santangelo. XRBcats: Galactic Low Mass X-ray Binary Catalogue. 3 2023.
- [51] R. Abbott et al. Model-based Cross-correlation Search for Gravitational Waves from the Low-mass X-Ray Binary Scorpius X-1 in LIGO O3 Data. *Astrophys. J. Lett.*, 941(2):L30, 2022.
- [52] R. N. Manchester. Millisecond Pulsars, their Evolution and Applications. *J. Astrophys. Astron.*, 38:42, 2017.
- [53] G. Woan, M. D. Pitkin, B. Haskell, D. I. Jones, and P. D. Lasky. Evidence for a Minimum Ellipticity in Millisecond Pulsars. *Astrophys. J. Lett.*, 863(2):L40, 2018.
- [54] R. N. Manchester, G. B. Hobbs, A. Teoh, and M. Hobbs. The Australia Telescope National Facility pulsar catalogue. *Astron. J.*, 129:1993, 2005. <http://www.atnf.csiro.au/research/pulsar/psrcat>.
- [55] R. Smits, M. Kramer, B. Stappers, D. R. Lorimer, J. Cordes, and A. Faulkner. Pulsar searches and timing with the square kilometre array. *Astron. Astrophys.*, 493:1161–1170, 2009.
- [56] D. I. Jones. Learning from the Frequency Content of Continuous Gravitational Wave Signals. 11 2021.
- [57] Magdalena Sieniawska, David Ian Jones, and Andrew Lawrence Miller. Measuring neutron star distances and properties with gravitational-wave parallax. *Mon. Not. Roy. Astron. Soc.*, 521(2):1924–1930, 2023.
- [58] Benjamin J. Owen. Maximum elastic deformations of compact stars with exotic equations of state. *Phys. Rev. Lett.*, 95:211101, 2005.
- [59] Phil Arras, Eanna E. Flanagan, Sharon M. Morsink, A. Katrin Schenk, Saul A. Teukolsky, and Ira Wasserman. Saturation of the  $R$  mode instability. *Astrophys. J.*, 591:1129–1151, 2003.

- [60] Nicolas Yunes and Frans Pretorius. Fundamental Theoretical Bias in Gravitational Wave Astrophysics and the Parameterized Post-Einsteinian Framework. *Phys. Rev. D*, 80:122003, 2009.
- [61] Nicolas Yunes, Kent Yagi, and Frans Pretorius. Theoretical Physics Implications of the Binary Black-Hole Mergers GW150914 and GW151226. *Phys. Rev. D*, 94(8):084002, 2016.
- [62] Scott E. Perkins, Nicolás Yunes, and Emanuele Berti. Probing Fundamental Physics with Gravitational Waves: The Next Generation. *Phys. Rev. D*, 103(4):044024, 2021.
- [63] L. Verde, T. Treu, and A. G. Riess. Tensions between the Early and the Late Universe. *Nature Astron.*, 3:891, 7 2019.
- [64] Eleonora Di Valentino, Olga Mena, Supriya Pan, Luca Visinelli, Weiqiang Yang, Alessandro Melchiorri, David F. Mota, Adam G. Riess, and Joseph Silk. In the realm of the Hubble tension—a review of solutions. *Class. Quant. Grav.*, 38(15):153001, 2021.
- [65] Adam G. Riess et al. A Comprehensive Measurement of the Local Value of the Hubble Constant with 1 km s<sup>-1</sup> Mpc<sup>-1</sup> Uncertainty from the Hubble Space Telescope and the SH0ES Team. *Astrophys. J. Lett.*, 934(1):L7, 2022.
- [66] N. Aghanim et al. Planck 2018 results. VI. Cosmological parameters. *Astron. Astrophys.*, 641:A6, 2020. [Erratum: *Astron. Astrophys.* 652, C4 (2021)].
- [67] B. P. Abbott et al. A gravitational-wave standard siren measurement of the Hubble constant. *Nature*, 551(7678):85–88, 2017.
- [68] Bernard F. Schutz. Determining the Hubble Constant from Gravitational Wave Observations. *Nature*, 323:310–311, 1986.
- [69] Antonella Palmese, Clecio R. Bom, Sunil Mucesh, and William G. Hartley. A Standard Siren Measurement of the Hubble Constant Using Gravitational-wave Events from the First Three LIGO/Virgo Observing Runs and the DESI Legacy Survey. *Astrophys. J.*, 943(1):56, 2023.
- [70] Atsushi Nishizawa. Measurement of Hubble constant with stellar-mass binary black holes. *Phys. Rev.*, D96(10):101303, 2017.
- [71] Ssohrab Borhanian, Arnab Dhani, Anuradha Gupta, K. G. Arun, and B. S. Sathyaprakash. Dark Sirens to Resolve the Hubble–Lemaître Tension. *Astrophys. J. Lett.*, 905(2):L28, 2020.
- [72] Ish Gupta. Using Gray Sirens to Resolve the Hubble–Lemaître Tension. 11 2022.
- [73] C. Messenger and J. Read. Measuring a cosmological distance-redshift relationship using only gravitational wave observations of binary neutron star coalescences. *Phys. Rev. Lett.*, 108:091101, 2012.
- [74] C. Messenger, Kentaro Takami, Sarah Gossan, Luciano Rezzolla, and B. S. Sathyaprakash. Source Redshifts from Gravitational-Wave Observations of Binary Neutron Star Mergers. *Phys. Rev. X*, 4(4):041004, 2014.
- [75] T. G. F. Li, W. Del Pozzo, and C. Messenger. Measuring the redshift of standard sirens using the neutron star deformability. In *13th Marcel Grossmann Meeting on Recent Developments in Theoretical and Experimental General Relativity, Astrophysics, and Relativistic Field Theories*, pages 2019–2021, 2015.
- [76] Walter Del Pozzo, Tjonnie G. F. Li, and Chris Messenger. Cosmological inference using only gravitational wave observations of binary neutron stars. *Phys. Rev. D*, 95(4):043502, 2017.
- [77] Deep Chatterjee, Abhishek Hegade K R, Gilbert Holder, Daniel E. Holz, Scott Perkins, Kent Yagi, and Nicolás Yunes. Cosmology with Love: Measuring the Hubble constant using neutron star universal relations. *Phys. Rev. D*, 104(8):083528, 2021.
- [78] Banafsheh Shiralilou, Geert Raaijmakers, Bastien Duboef, Samaya Nissanke, Francois Foucart, Tanja Hinderer, and Andrew Williamson. Measuring Hubble Constant with Dark Neutron Star-Black Hole Mergers. 7 2022.
- [79] Tathagata Ghosh, Bhaskar Biswas, and Sukanta Bose. Simultaneous inference of neutron star equation of state and the Hubble constant with a population of merging neutron stars. *Phys. Rev. D*, 106(12):123529, 2022.
- [80] Bo Wang, Zhenyu Zhu, Ang Li, and Wen Zhao. Comprehensive analysis of the tidal effect in gravitational waves and implication for cosmology. *Astrophys. J. Suppl.*, 250(1):6, 2020.
- [81] Shang-Jie Jin, Tian-Nuo Li, Jing-Fei Zhang, and Xin Zhang. Precisely measuring the Hubble constant and dark energy using only gravitational-wave dark sirens. 2 2022.
- [82] A. F. Heavens, M. Seikel, B. D. Nord, M. Aich, Y. Bouffanais, B. A. Bassett, and M. P. Hobson. Generalized Fisher matrices. *Mon. Not. Roy. Astron. Soc.*, 445(2):1687–1693, 2014.
- [83] A. Renske A. C. Wierda, Ewoud Wempe, Otto A. Hannuksela, L. éon V. E. Koopmans, and Chris Van Den Broeck. Beyond the Detector Horizon: Forecasting Gravitational-Wave Strong Lensing. *Astrophys. J.*, 921(2):154, 2021.
- [84] R. Abbott et al. Search for Lensing Signatures in the Gravitational-Wave Observations from the First Half of LIGO–Virgo’s Third Observing Run. *Astrophys. J.*, 923(1):14, 2021.
- [85] R. Abbott et al. Search for gravitational-lensing signatures in the full third observing run of the LIGO–Virgo network. 4 2023.
- [86] Bruce Allen and Joseph D. Romano. Detecting a stochastic background of gravitational radiation: Signal processing strategies and sensitivities. *Phys. Rev. D*, 59:102001, 1999.
- [87] Joseph D. Romano and Neil J. Cornish. Detection methods for stochastic gravitational-wave backgrounds: a unified treatment. *Living Rev. Rel.*, 20(1):2, 2017.
- [88] Eanna E. Flanagan. The Sensitivity of the laser interferometer gravitational wave observatory (LIGO) to a stochastic background, and its dependence on the detector orientations. *Phys. Rev. D*, 48:2389–2407, 1993.
- [89] Nelson Christensen. Stochastic Gravitational Wave Backgrounds. *Rept. Prog. Phys.*, 82(1):016903, 2019.
- [90] Eric Thrane and Joseph D. Romano. Sensitivity curves for searches for gravitational-wave backgrounds. *Phys. Rev. D*, 88(12):124032, 2013.
- [91] J. Aasi et al. Searching for stochastic gravitational waves using data from the two colocated LIGO Hanford detectors. *Phys. Rev. D*, 91(2):022003, 2015.
- [92] Ashish Sharma and Jan Harms. Searching for cosmological gravitational-wave backgrounds with third-generation detectors in the presence of an astrophysical foreground. *Phys. Rev. D*, 102(6):063009, September 2020.

- [93] Sylvia Biscoveanu, Colm Talbot, Eric Thrane, and Rory Smith. Measuring the Primordial Gravitational-Wave Background in the Presence of Astrophysical Foregrounds. *Phys. Rev. Lett.*, 125(24):241101, December 2020.
- [94] Arianna I. Renzini, Boris Goncharov, Alexander C. Jenkins, and Patrick M. Meyers. Stochastic Gravitational-Wave Backgrounds: Current Detection Efforts and Future Prospects. *Galaxies*, 10(1):34, February 2022.
- [95] Bei Zhou, Luca Reali, Emanuele Berti, Mesut Çalişkan, Cyril Creque-Sarbinowski, Marc Kamionkowski, and B. S. Sathyaprakash. Subtracting Compact Binary Foregrounds to Search for Subdominant Gravitational-Wave Backgrounds in Next-Generation Ground-Based Observatories. *arXiv e-prints*, page arXiv:2209.01310, September 2022.
- [96] Haowen Zhong, Rich Ormiston, and Vuk Mandic. Detecting cosmological gravitational wave background after removal of compact binary coalescences in future gravitational wave detectors. *Phys. Rev. D*, 107(6):064048, March 2023.
- [97] Richard Brito, Vitor Cardoso, and Paolo Pani. Super-radiance: New Frontiers in Black Hole Physics. *Lect. Notes Phys.*, 906:pp.1–237, 2015.
- [98] Asimina Arvanitaki, Masha Baryakhtar, Savvas Dimopoulos, Sergei Dubovsky, and Robert Lasenby. Black Hole Mergers and the QCD Axion at Advanced LIGO. *Phys. Rev. D*, 95(4):043001, 2017.
- [99] Richard Brito, Shrobona Ghosh, Enrico Barausse, Emanuele Berti, Vitor Cardoso, Irina Dvorkin, Antoine Klein, and Paolo Pani. Gravitational wave searches for ultralight bosons with LIGO and LISA. *Phys. Rev. D*, 96(6):064050, 2017.
- [100] R. Abbott et al. All-sky search for gravitational wave emission from scalar boson clouds around spinning black holes in LIGO O3 data. *Phys. Rev. D*, 105(10):102001, 2022.
- [101] Pia Astone, Alberto Colla, Sabrina D’Antonio, Sergio Frasca, and Cristiano Palomba. Method for all-sky searches of continuous gravitational wave signals using the frequency-Hough transform. *Phys. Rev. D*, 90(4):042002, 2014.
- [102] Marica Branchesi et al. Science with the Einstein Telescope: a comparison of different designs. 3 2023.
- [103] S. A. Sanidas, R. A. Battye, and B. W. Stappers. Constraints on cosmic string tension imposed by the limit on the stochastic gravitational wave background from the European Pulsar Timing Array. *Phys. Rev. D*, 85:122003, 2012.
- [104] Richard Easther, Jr. Giblin, John T., and Eugene A. Lim. Gravitational Wave Production at the End of Inflation. *Phys. Rev. Lett.*, 99(22):221301, November 2007.